UC Berkeley
UC Berkeley Previously Published Works

Title

Improved measurement of the CKM angle γ in B∓→D(*)K(*)∓ decays with a Dalitz plot analysis of D decays to KS0π+π- and KS0K+K-

Permalink

https://escholarship.org/uc/item/7g2371dz

Journal

Physical Review D, 78(3)

ISSN

2470-0010

Authors

Aubert, B
Bona, M
Karyotakis, Y
et al.

Publication Date

2008-08-01

DOI

10.1103/physrevd.78.034023

Copyright Information

Peer reviewed

Improved measurement of the CKM angle γ in $B^{\mp} \to D^{(*)}K^{(*)\mp}$ decays with a Dalitz plot analysis of D decays to $K_S^0\pi^+\pi^-$ and $K_S^0K^+K^-$

B. Aubert,[1] M. Bona,[1] Y. Karyotakis,[1] J. P. Lees,[1] V. Poireau,[1] E. Prencipe,[1] X. Prudent,[1] V. Tisserand,[1] J. Garra Tico,[2] E. Grauges,[2] L. Lopez,[3] A. Palano,[3] M. Pappagallo,[3] G. Eigen,[4] B. Stugu,[4] L. Sun,[4] G. S. Abrams,[5] M. Battaglia,[5] D. N. Brown,[5] J. Button-Shafer,[5] R. N. Cahn,[5] R. G. Jacobsen,[5] J. A. Kadyk,[5] L. T. Kerth,[5] Yu. G. Kolomensky,[5] G. Kukartsev,[5] G. Lynch,[5] I. L. Osipenkov,[5] M. T. Ronan,[5,*] K. Tackmann,[5] T. Tanabe,[5] W. A. Wenzel,[5] C. M. Hawkes,[6] N. Soni,[6] A. T. Watson,[6] H. Koch,[7] T. Schroeder,[7] D. Walker,[8] D. J. Asgeirsson,[9] T. Cuhadar-Donszelmann,[9] B. G. Fulsom,[9] C. Hearty,[9] T. S. Mattison,[9] J. A. McKenna,[9] M. Barrett,[10] A. Khan,[10] M. Saleem,[10] L. Teodorescu,[10] V. E. Blinov,[11] A. D. Bukin,[11] A. R. Buzykaev,[11] V. P. Druzhinin,[11] V. B. Golubev,[11] A. P. Onuchin,[11] S. I. Serednyakov,[11] Yu. I. Skovpen,[11] E. P. Solodov,[11] K. Yu. Todyshev,[11] M. Bondioli,[12] S. Curry,[12] I. Eschrich,[12] D. Kirkby,[12] A. J. Lankford,[12] P. Lund,[12] M. Mandelkern,[12] E. C. Martin,[12] D. P. Stoker,[12] S. Abachi,[13] C. Buchanan,[13] J. W. Gary,[14] F. Liu,[14] O. Long,[14] B. C. Shen,[14,*] G. M. Vitug,[14] Z. Yasin,[14] L. Zhang,[14] V. Sharma,[15] C. Campagnari,[16] T. M. Hong,[16] D. Kovalskyi,[16] M. A. Mazur,[16] J. D. Richman,[16] T. W. Beck,[17] A. M. Eisner,[17] C. J. Flacco,[17] C. A. Heusch,[17] J. Kroseberg,[17] W. S. Lockman,[17] T. Schalk,[17] B. A. Schumm,[17] A. Seiden,[17] L. Wang,[17] M. G. Wilson,[17] L. O. Winstrom,[17] C. H. Cheng,[18] D. A. Doll,[18] B. Echenard,[18] F. Fang,[18] D. G. Hitlin,[18] I. Narsky,[18] T. Piatenko,[18] F. C. Porter,[18] R. Andreassen,[19] G. Mancinelli,[19] B. T. Meadows,[19] K. Mishra,[19] M. D. Sokoloff,[19] F. Blanc,[20] P. C. Bloom,[20] W. T. Ford,[20] A. Gaz,[20] J. F. Hirschauer,[20] A. Kreisel,[20] M. Nagel,[20] U. Nauenberg,[20] A. Olivas,[20] J. G. Smith,[20] K. A. Ulmer,[20] S. R. Wagner,[20] R. Ayad,[21,+] A. M. Gabareen,[21] A. Soffer,[21,‡] W. H. Toki,[21] R. J. Wilson,[21] D. D. Altenburg,[22] E. Feltresi,[22] A. Hauke,[22] H. Jasper,[22] M. Karbach,[22] J. Merkel,[22] A. Petzold,[22] B. Spaan,[22] K. Wacker,[22] V. Klose,[23] M. J. Kobel,[23] H. M. Lacker,[23] W. F. Mader,[23] R. Nogowski,[23] K. R. Schubert,[23] R. Schwierz,[23] J. E. Sundermann,[23] A. Volk,[23] D. Bernard,[24] G. R. Bonneaud,[24] E. Latour,[24] Ch. Thiebaux,[24] M. Verderi,[24] P. J. Clark,[25] W. Gradl,[25] S. Playfer,[25] J. E. Watson,[25] M. Andreotti,[26] D. Bettoni,[26] C. Bozzi,[26] R. Calabrese,[26] A. Cecchi,[26] G. Cibinetto,[26] P. Franchini,[26] E. Luppi,[26] M. Negrini,[26] A. Petrella,[26] L. Piemontese,[26] V. Santoro,[26] F. Anulli,[27] R. Baldini-Ferroli,[27] A. Calcaterra,[27] R. de Sangro,[27] G. Finocchiaro,[27] S. Pacetti,[27] P. Patteri,[27] I. M. Peruzzi,[27,§] M. Piccolo,[27] M. Rama,[27] A. Zallo,[27] A. Buzzo,[28] R. Contri,[28] M. Lo Vetere,[28] M. M. Macri,[28] M. R. Monge,[28] S. Passaggio,[28] C. Patrignani,[28] E. Robutti,[28] A. Santroni,[28] S. Tosi,[28] K. S. Chaisanguanthum,[29] M. Morii,[29] R. S. Dubitzky,[30] J. Marks,[30] S. Schenk,[30] U. Uwer,[30] D. J. Bard,[31] P. D. Dauncey,[31] J. A. Nash,[31] W. Panduro Vazquez,[31] M. Tibbetts,[31] P. K. Behera,[32] X. Chai,[32] M. J. Charles,[32] U. Mallik,[32] J. Cochran,[33] H. B. Crawley,[33] L. Dong,[33] W. T. Meyer,[33] S. Prell,[33] E. I. Rosenberg,[33] A. E. Rubin,[33] Y. Y. Gao,[34] A. V. Gritsan,[34] Z. J. Guo,[34] C. K. Lae,[34] A. G. Denig,[35] M. Fritsch,[35] G. Schott,[35] N. Arnaud,[36] J. Béquilleux,[36] A. D'Orazio,[36] M. Davier,[36] J. Firmino da Costa,[36] G. Grosdidier,[36] A. Höcker,[36] V. Lepeltier,[36] F. Le Diberder,[36] A. M. Lutz,[36] S. Pruvot,[36] P. Roudeau,[36] M. H. Schune,[36] J. Serrano,[36] V. Sordini,[36] A. Stocchi,[36] W. F. Wang,[36] G. Wormser,[36] D. J. Lange,[37] D. M. Wright,[37] I. Bingham,[38] J. P. Burke,[38] C. A. Chavez,[38] J. R. Fry,[38] E. Gabathuler,[38] R. Gamet,[38] D. E. Hutchcroft,[38] D. J. Payne,[38] C. Touramanis,[38] A. J. Bevan,[39] K. A. George,[39] F. Di Lodovico,[39] R. Sacco,[39] M. Sigamani,[39] G. Cowan,[40] H. U. Flaecher,[40] D. A. Hopkins,[40] S. Paramesvaran,[40] F. Salvatore,[40] A. C. Wren,[40] D. N. Brown,[41] C. L. Davis,[41] K. E. Alwyn,[42] N. R. Barlow,[42] R. J. Barlow,[42] Y. M. Chia,[42] C. L. Edgar,[42] G. D. Lafferty,[42] T. J. West,[42] J. I. Yi,[42] J. Anderson,[43] C. Chen,[43] A. Jawahery,[43] D. A. Roberts,[43] G. Simi,[43] J. M. Tuggle,[43] C. Dallapiccola,[44] S. S. Hertzbach,[44] X. Li,[44] E. Salvati,[44] S. Saremi,[44] R. Cowan,[45] D. Dujmic,[45] P. H. Fisher,[45] K. Koeneke,[45] G. Sciolla,[45] M. Spitznagel,[45] F. Taylor,[45] R. K. Yamamoto,[45] M. Zhao,[45] S. E. Mclachlin,[46,*] P. M. Patel,[46] S. H. Robertson,[46] A. Lazzaro,[47] V. Lombardo,[47] F. Palombo,[47] J. M. Bauer,[48] L. Cremaldi,[48] V. Eschenburg,[48] R. Godang,[48] R. Kroeger,[48] D. A. Sanders,[48] D. J. Summers,[48] H. W. Zhao,[48] S. Brunet,[49] D. Côté,[49] M. Simard,[49] P. Taras,[49] F. B. Viaud,[49] H. Nicholson,[50] G. De Nardo,[51] L. Lista,[51] D. Monorchio,[51] C. Sciacca,[51] M. A. Baak,[52] G. Raven,[52] H. L. Snoek,[52] C. P. Jessop,[53] K. J. Knoepfel,[53] J. M. LoSecco,[53] G. Benelli,[54] L. A. Corwin,[54] K. Honscheid,[54] H. Kagan,[54] R. Kass,[54] J. P. Morris,[54] A. M. Rahimi,[54] J. J. Regensburger,[54] S. J. Sekula,[54] Q. K. Wong,[54] N. L. Blount,[55] J. Brau,[55] R. Frey,[55] O. Igonkina,[55] J. A. Kolb,[55] M. Lu,[55] R. Rahmat,[55] N. B. Sinev,[55] D. Strom,[55] J. Strube,[55] E. Torrence,[55] G. Castelli,[56] N. Gagliardi,[56] M. Margoni,[56] M. Morandin,[56] M. Posocco,[56] M. Rotondo,[56] F. Simonetto,[56] R. Stroili,[56] C. Voci,[56] P. del Amo Sanchez,[57] E. Ben-Haim,[57] H. Briand,[57] G. Calderini,[57] J. Chauveau,[57] P. David,[57] L. Del Buono,[57] O. Hamon,[57] Ph. Leruste,[57] J. Ocariz,[57] A. Perez,[57] J. Prendki,[57] L. Gladney,[58] M. Biasini,[59] R. Covarelli,[59] E. Manoni,[59] C. Angelini,[60] G. Batignani,[60] S. Bettarini,[60] M. Carpinelli,[60,‖] A. Cervelli,[60] F. Forti,[60] M. A. Giorgi,[60] A. Lusiani,[60] G. Marchiori,[60] M. Morganti,[60] N. Neri,[60] E. Paoloni,[60] G. Rizzo,[60] J. J. Walsh,[60] J. Biesiada,[61] D. Lopes Pegna,[61] C. Lu,[61] J. Olsen,[61]

A. J. S. Smith,[61] A. V. Telnov,[61] E. Baracchini,[62] G. Cavoto,[62] D. del Re,[62] E. Di Marco,[62] R. Faccini,[62] F. Ferrarotto,[62] F. Ferroni,[62] M. Gaspero,[62] P. D. Jackson,[62] L. Li Gioi,[62] M. A. Mazzoni,[62] S. Morganti,[62] G. Piredda,[62] F. Polci,[62] F. Renga,[62] C. Voena,[62] M. Ebert,[63] T. Hartmann,[63] H. Schröder,[63] R. Waldi,[63] T. Adye,[64] B. Franek,[64] E. O. Olaiya,[64] W. Roethel,[64] F. F. Wilson,[64] S. Emery,[65] M. Escalier,[65] L. Esteve,[65] A. Gaidot,[65] S. F. Ganzhur,[65] G. Hamel de Monchenault,[65] W. Kozanecki,[65] G. Vasseur,[65] Ch. Yèche,[65] M. Zito,[65] X. R. Chen,[66] H. Liu,[66] W. Park,[66] M. V. Purohit,[66] R. M. White,[66] J. R. Wilson,[66] M. T. Allen,[67] D. Aston,[67] R. Bartoldus,[67] P. Bechtle,[67] J. F. Benitez,[67] R. Cenci,[67] J. P. Coleman,[67] M. R. Convery,[67] J. C. Dingfelder,[67] J. Dorfan,[67] G. P. Dubois-Felsmann,[67] W. Dunwoodie,[67] R. C. Field,[67] S. J. Gowdy,[67] M. T. Graham,[67] P. Grenier,[67] C. Hast,[67] W. R. Innes,[67] J. Kaminski,[67] M. H. Kelsey,[67] H. Kim,[67] P. Kim,[67] M. L. Kocian,[67] D. W. G. S. Leith,[67] S. Li,[67] B. Lindquist,[67] S. Luitz,[67] V. Luth,[67] H. L. Lynch,[67] D. B. MacFarlane,[67] H. Marsiske,[67] R. Messner,[67] D. R. Muller,[67] H. Neal,[67] S. Nelson,[67] C. P. O'Grady,[67] I. Ofte,[67] A. Perazzo,[67] M. Perl,[67] B. N. Ratcliff,[67] A. Roodman,[67] A. A. Salnikov,[67] R. H. Schindler,[67] J. Schwiening,[67] A. Snyder,[67] D. Su,[67] M. K. Sullivan,[67] K. Suzuki,[67] S. K. Swain,[67] J. M. Thompson,[67] J. Va'vra,[67] A. P. Wagner,[67] M. Weaver,[67] C. A. West,[67] W. J. Wisniewski,[67] M. Wittgen,[67] D. H. Wright,[67] H. W. Wulsin,[67] A. K. Yarritu,[67] K. Yi,[67] C. C. Young,[67] V. Ziegler,[67] P. R. Burchat,[68] A. J. Edwards,[68] S. A. Majewski,[68] T. S. Miyashita,[68] B. A. Petersen,[68] L. Wilden,[68] S. Ahmed,[69] M. S. Alam,[69] R. Bula,[69] J. A. Ernst,[69] B. Pan,[69] M. A. Saeed,[69] S. B. Zain,[69] S. M. Spanier,[70] B. J. Wogsland,[70] R. Eckmann,[71] J. L. Ritchie,[71] A. M. Ruland,[71] C. J. Schilling,[71] R. F. Schwitters,[71] B. W. Drummond,[72] J. M. Izen,[72] X. C. Lou,[72] S. Ye,[72] F. Bianchi,[73] D. Gamba,[73] M. Pelliccioni,[73] M. Bomben,[74] L. Bosisio,[74] C. Cartaro,[74] G. Della Ricca,[74] L. Lanceri,[74] L. Vitale,[74] V. Azzolini,[75] N. Lopez-March,[75] F. Martinez-Vidal,[75] D. A. Milanes,[75] A. Oyanguren,[75] J. Albert,[76] Sw. Banerjee,[76] B. Bhuyan,[76] H. H. F. Choi,[76] K. Hamano,[76] R. Kowalewski,[76] M. J. Lewczuk,[76] I. M. Nugent,[76] J. M. Roney,[76] R. J. Sobie,[76] T. J. Gershon,[77] P. F. Harrison,[77] J. Ilic,[77] T. E. Latham,[77] G. B. Mohanty,[77] H. R. Band,[78] X. Chen,[78] S. Dasu,[78] K. T. Flood,[78] Y. Pan,[78] M. Pierini,[78] R. Prepost,[78] C. O. Vuosalo,[78] and S. L. Wu[78]

(*BABAR* Collaboration)

[1]*Laboratoire de Physique des Particules, IN2P3/CNRS et Université de Savoie, F-74941 Annecy-Le-Vieux, France*
[2]*Universitat de Barcelona, Facultat de Fisica, Departament ECM, E-08028 Barcelona, Spain*
[3]*Università di Bari, Dipartimento di Fisica and INFN, I-70126 Bari, Italy*
[4]*University of Bergen, Institute of Physics, N-5007 Bergen, Norway*
[5]*Lawrence Berkeley National Laboratory and University of California, Berkeley, California 94720, USA*
[6]*University of Birmingham, Birmingham, B15 2TT, United Kingdom*
[7]*Ruhr Universität Bochum, Institut für Experimentalphysik 1, D-44780 Bochum, Germany*
[8]*University of Bristol, Bristol BS8 1TL, United Kingdom*
[9]*University of British Columbia, Vancouver, British Columbia, Canada V6T 1Z1*
[10]*Brunel University, Uxbridge, Middlesex UB8 3PH, United Kingdom*
[11]*Budker Institute of Nuclear Physics, Novosibirsk 630090, Russia*
[12]*University of California at Irvine, Irvine, California 92697, USA*
[13]*University of California at Los Angeles, Los Angeles, California 90024, USA*
[14]*University of California at Riverside, Riverside, California 92521, USA*
[15]*University of California at San Diego, La Jolla, California 92093, USA*
[16]*University of California at Santa Barbara, Santa Barbara, California 93106, USA*
[17]*University of California at Santa Cruz, Institute for Particle Physics, Santa Cruz, California 95064, USA*
[18]*California Institute of Technology, Pasadena, California 91125, USA*
[19]*University of Cincinnati, Cincinnati, Ohio 45221, USA*
[20]*University of Colorado, Boulder, Colorado 80309, USA*
[21]*Colorado State University, Fort Collins, Colorado 80523, USA*
[22]*Technische Universität Dortmund, Fakultät Physik, D-44221 Dortmund, Germany*
[23]*Technische Universität Dresden, Institut für Kern- und Teilchenphysik, D-01062 Dresden, Germany*
[24]*Laboratoire Leprince-Ringuet, CNRS/IN2P3, Ecole Polytechnique, F-91128 Palaiseau, France*
[25]*University of Edinburgh, Edinburgh EH9 3JZ, United Kingdom*
[26]*Università di Ferrara, Dipartimento di Fisica and INFN, I-44100 Ferrara, Italy*
[27]*Laboratori Nazionali di Frascati dell'INFN, I-00044 Frascati, Italy*
[28]*Università di Genova, Dipartimento di Fisica and INFN, I-16146 Genova, Italy*
[29]*Harvard University, Cambridge, Massachusetts 02138, USA*
[30]*Universität Heidelberg, Physikalisches Institut, Philosophenweg 12, D-69120 Heidelberg, Germany*
[31]*Imperial College London, London, SW7 2AZ, United Kingdom*

[32]*University of Iowa, Iowa City, Iowa 52242, USA*

[33]*Iowa State University, Ames, Iowa 50011-3160, USA*

[34]*Johns Hopkins University, Baltimore, Maryland 21218, USA*

[35]*Universität Karlsruhe, Institut für Experimentelle Kernphysik, D-76021 Karlsruhe, Germany*

[36]*Laboratoire de l'Accélérateur Linéaire, IN2P3/CNRS et Université Paris-Sud 11,*
Centre Scientifique d'Orsay, B.P. 34, F-91898 ORSAY Cedex, France

[37]*Lawrence Livermore National Laboratory, Livermore, California 94550, USA*

[38]*University of Liverpool, Liverpool L69 7ZE, United Kingdom*

[39]*Queen Mary, University of London, E1 4NS, United Kingdom*

[40]*University of London, Royal Holloway and Bedford New College, Egham, Surrey TW20 0EX, United Kingdom*

[41]*University of Louisville, Louisville, Kentucky 40292, USA*

[42]*University of Manchester, Manchester M13 9PL, United Kingdom*

[43]*University of Maryland, College Park, Maryland 20742, USA*

[44]*University of Massachusetts, Amherst, Massachusetts 01003, USA*

[45]*Massachusetts Institute of Technology, Laboratory for Nuclear Science, Cambridge, Massachusetts 02139, USA*

[46]*McGill University, Montréal, Québec, Canada H3A 2T8*

[47]*Università di Milano, Dipartimento di Fisica and INFN, I-20133 Milano, Italy*

[48]*University of Mississippi, University, Mississippi 38677, USA*

[49]*Université de Montréal, Physique des Particules, Montréal, Québec, Canada H3C 3J7*

[50]*Mount Holyoke College, South Hadley, Massachusetts 01075, USA*

[51]*Università di Napoli Federico II, Dipartimento di Scienze Fisiche and INFN, I-80126, Napoli, Italy*

[52]*NIKHEF, National Institute for Nuclear Physics and High Energy Physics, NL-1009 DB Amsterdam, The Netherlands*

[53]*University of Notre Dame, Notre Dame, Indiana 46556, USA*

[54]*The Ohio State University, Columbus, Ohio 43210, USA*

[55]*University of Oregon, Eugene, Oregon 97403, USA*

[56]*Università di Padova, Dipartimento di Fisica and INFN, I-35131 Padova, Italy*

[57]*Laboratoire de Physique Nucléaire et de Hautes Energies, IN2P3/CNRS,*
Université Pierre et Marie Curie-Paris6, Université Denis Diderot-Paris7, F-75252 Paris, France

[58]*University of Pennsylvania, Philadelphia, Pennsylvania 19104, USA*

[59]*Università di Perugia, Dipartimento di Fisica and INFN, I-06100 Perugia, Italy*

[60]*Università di Pisa, Dipartimento di Fisica, Scuola Normale Superiore and INFN, I-56127 Pisa, Italy*

[61]*Princeton University, Princeton, New Jersey 08544, USA*

[62]*Università di Roma La Sapienza, Dipartimento di Fisica and INFN, I-00185 Roma, Italy*

[63]*Universität Rostock, D-18051 Rostock, Germany*

[64]*Rutherford Appleton Laboratory, Chilton, Didcot, Oxon, OX11 0QX, United Kingdom*

[65]*DSM/Dapnia, CEA/Saclay, F-91191 Gif-sur-Yvette, France*

[66]*University of South Carolina, Columbia, South Carolina 29208, USA*

[67]*Stanford Linear Accelerator Center, Stanford, California 94309, USA*

[68]*Stanford University, Stanford, California 94305-4060, USA*

[69]*State University of New York, Albany, New York 12222, USA*

[70]*University of Tennessee, Knoxville, Tennessee 37996, USA*

[71]*University of Texas at Austin, Austin, Texas 78712, USA*

[72]*University of Texas at Dallas, Richardson, Texas 75083, USA*

[73]*Università di Torino, Dipartimento di Fisica Sperimentale and INFN, I-10125 Torino, Italy*

[74]*Università di Trieste, Dipartimento di Fisica and INFN, I-34127 Trieste, Italy*

[75]*IFIC, Universitat de Valencia-CSIC, E-46071 Valencia, Spain*

[76]*University of Victoria, Victoria, British Columbia, Canada V8W 3P6*

[77]*Department of Physics, University of Warwick, Coventry CV4 7AL, United Kingdom*

[78]*University of Wisconsin, Madison, Wisconsin 53706, USA*

We report on an improved measurement of the Cabibbo-Kobayashi-Maskawa *CP*-violating phase γ through a Dalitz plot analysis of neutral *D* meson decays to $K_S^0 \pi^+ \pi^-$ and $K_S^0 K^+ K^-$ produced in the processes $B^\mp \to DK^\mp$, $B^\mp \to D^* K^\mp$ with $D^* \to D\pi^0$, $D\gamma$, and $B^\mp \to DK^{*\mp}$ with $K^{*\mp} \to K_S^0 \pi^\mp$. Using a sample of 383×10^6 $B\bar{B}$ pairs collected by the *BABAR* detector, we measure $\gamma = (76 \pm 22 \pm 5 \pm 5)°$

*Deceased.

[+]Present address: Temple University, Philadelphia, PA 19122, USA.

[‡]Present address: Tel Aviv University, Tel Aviv, 69978, Israel.

[§]Also at Università di Perugia, Dipartimento di Fisica, Perugia, Italy.

[‖]Also at Università di Sassari, Sassari, Italy.

(mod 180°), where the first error is statistical, the second is the experimental systematic uncertainty, and the third reflects the uncertainty on the description of the Dalitz plot distributions. The corresponding 2-standard-deviation region is $29° < \gamma < 122°$. This result has a significance of direct CP violation ($\gamma \neq 0$) of 3.0 standard deviations.

I. INTRODUCTION AND OVERVIEW

In the standard model (SM) the phase in the Cabibbo-Kobayashi-Maskawa (CKM) quark-mixing matrix [1] is the sole source of CP violation in the quark sector of the electroweak interactions. This phase can be directly determined using a variety of methods, involving either the interference between decays with and without mixing in time-dependent CP asymmetries in neutral B meson decays, or interference between neutral B (self-tagged) or charged B decays yielding the same final state (direct CP violation). These multiple determinations in CP-violating tree-level processes as well as in decays involving penguin diagrams test the CKM mechanism, thus probing the presence of physics beyond the SM [2].

Among these determinations, the measurement of the angle γ, defined as $\arg[-V_{ud}V_{ub}^*/V_{cd}V_{cb}^*]$, where V_{ij} are the elements of the CKM matrix, is one of the most difficult to achieve and constitutes an important goal of present and future B physics experiments. Several methods have been proposed to extract γ. However, those using $B^{\mp} \to \tilde{D}^{(*)0}K^{(*)\mp}$ decays [3,4] (the symbol $\tilde{D}^{(*)0}$ indicates either a $D^{(*)0}$ or a $\bar{D}^{(*)0}$ meson) are theoretically clean and are unlikely to be affected by new physics because the main contributions to the amplitudes come from tree-level diagrams, as shown in Fig. 1. This is an important distinction from most of the other direct measurements of phases of CKM elements. The decay amplitudes for the color allowed $B^- \to D^{(*)0}K^{(*)-}$ ($b \to c\bar{u}s$) and the color suppressed $B^- \to \bar{D}^{(*)0}K^{(*)-}$ ($b \to u\bar{c}s$) transitions [5] differ by a factor $r_B^{(*)}e^{i(\delta_B^{(*)}\mp\gamma)}$. Here, $r_B^{(*)}$ is the magnitude of the ratio of the amplitudes $\mathcal{A}(B^- \to \bar{D}^{(*)0}K^-)$ and $\mathcal{A}(B^- \to D^{(*)0}K^-)$ and $\delta_B^{(*)}$ is their relative strong phase. The weak phase γ leads to different B^- and B^+ decay rates (direct CP violation) and, when the $D^{(*)0}$ and $\bar{D}^{(*)0}$ decay to a

common final state [6–9], the phases become observable. The uncertainty in γ scales roughly as $1/r_B^{(*)}$. From the ratio of CKM matrix elements we expect $r_B^{(*)} \approx c_F \mid V_{cs}V_{ub}^* \mid / \mid V_{us}V_{cb}^* \mid$ to be approximately in the range 0.1–0.2, where $c_F \sim 0.2$–0.4 is the color suppression factor [10,11].

When the neutral D meson is reconstructed in a three-body final state, such as $K_S^0\pi^+\pi^-$, the distribution in the Dalitz plot [12] depends on the interference between Cabibbo allowed, doubly Cabibbo suppressed, and CP-eigenstate decay amplitudes of D^0 (from $B^{\mp} \to D^{(*)0}K^{(*)\mp}$) and $\bar{D}^0$ (from $B^{\mp} \to \bar{D}^{(*)0}K^{(*)\mp}$). The dominant interfering amplitudes in the $K_S^0\pi^+\pi^-$ final state are $D^0 \to K^{*-}\pi^+$, $D^0 \to K^{*+}\pi^-$, and $D^0 \to K_S^0\rho(770)^0$ [5,13]. Neglecting effects from $D^0 - \bar{D}^0$ mixing and CP asymmetries in neutral D decays that are 1% or less [14–16], the $B^{\mp} \to \tilde{D}^{(*)0}K^{\mp}$, with $\tilde{D}^{*0} \to \tilde{D}^0\pi^0$, $\tilde{D}^0\gamma$, $\tilde{D}^0 \to K_S^0\pi^+\pi^-$ decay chain amplitude $\mathcal{A}_{\mp}^{(*)}(m_-^2, m_+^2)$ can be written as

$$\mathcal{A}_{\mp}^{(*)}(m_-^2, m_+^2) \propto \mathcal{A}_{D\mp} + \lambda r_B^{(*)}e^{i(\delta_B^{(*)}\mp\gamma)}\mathcal{A}_{D\pm}, \quad (1)$$

where m_-^2 and m_+^2 are the squared invariant masses of the $K_S^0\pi^-$ and $K_S^0\pi^+$ combinations, respectively, and $\mathcal{A}_{D\mp} \equiv \mathcal{A}_D(m_\mp^2, m_\pm^2)$, with $\mathcal{A}_{D-}$ ($\mathcal{A}_{D+}$) the amplitude of the $D^0 \to K_S^0\pi^+\pi^-$ ($\bar{D}^0 \to K_S^0\pi^-\pi^+$) decay. For convenience, m_0^2 is defined analogously for the $\pi^+\pi^-$ combination. The factor λ in Eq. (1) takes the value -1 for the decay $B^{\mp} \to \tilde{D}^{*0}[\bar{D}^0\gamma]K^{\mp}$ and $+1$ for the remaining B decays. This relative sign arises due to charge conjugation and angular momentum conservation in the $\tilde{D}^{*0}$ decay [17]. The corresponding decay rate $\Gamma_{\mp}^{(*)}(m_-^2, m_+^2)$ can therefore be written as

$$\begin{aligned}\Gamma_{\mp}^{(*)}(m_-^2, m_+^2) \propto\ &|\mathcal{A}_{D\mp}|^2 + r_B^{(*)2}|\mathcal{A}_{D\pm}|^2 \\ &+ 2\lambda[x_{\mp}^{(*)}\Re\{\mathcal{A}_{D\mp}\mathcal{A}_{D\pm}^*\} \\ &+ y_{\mp}^{(*)}\Im\{\mathcal{A}_{D\mp}\mathcal{A}_{D\pm}^*\}], \quad (2)\end{aligned}$$

where we introduce the CP parameters [18] $x_{\mp}^{(*)} = r_B^{(*)}\cos(\delta_B^{(*)}\mp\gamma)$ and $y_{\mp}^{(*)} = r_B^{(*)}\sin(\delta_B^{(*)}\mp\gamma)$, where $x_{\mp}^{(*)2} + y_{\mp}^{(*)2} = r_B^{(*)2}$.

Decays $B^{\mp} \to \tilde{D}^0K^{*\mp}$ with $K^{*\mp} \to K_S^0\pi^{\mp}$ [4] are also used in this analysis. For these, Eq. (2) requires the replacements $\Gamma_{\mp}^{(*)} \to \Gamma_{s\mp}$, $r_B^{(*)} \to r_s$, $\delta_B^{(*)} \to \delta_s$, $x_{\mp}^{(*)} \to x_{s\mp} = \kappa r_s\cos(\delta_s \mp \gamma)$, and $y_{\mp}^{(*)} \to y_{s\mp} = \kappa r_s\sin(\delta_s \mp \gamma)$, where $x_{s\mp}^2 + y_{s\mp}^2 = \kappa^2 r_s^2$, where [11]
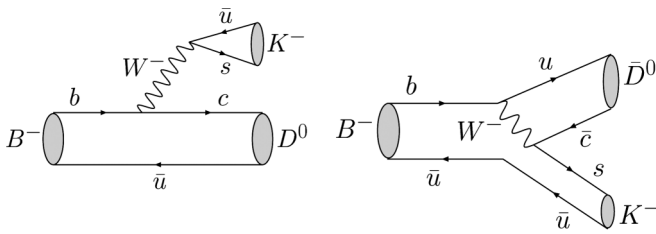

FIG. 1. Main Feynman diagrams contributing to the $B^- \to \tilde{D}^0K^-$ decay. The left diagram proceeds via $b \to c\bar{u}s$ transition, while the right diagram proceeds via $b \to u\bar{c}s$ transition and is color suppressed.

$$r_s^2 = \frac{\int A_u^2(p)\mathrm{d}p}{\int A_c^2(p)\mathrm{d}p}, \qquad \kappa e^{i\delta_s} = \frac{\int A_c(p)A_u(p)e^{i\delta(p)}\mathrm{d}p}{\sqrt{\int A_c^2(p)\mathrm{d}p \int A_u^2(p)\mathrm{d}p}}.$$

(3)

Here, $A_c(p)$ and $A_u(p)$ are the magnitudes of the $b \to c$ and $b \to u$ amplitudes as a function of the $B^{\mp} \to \tilde{D}^0 K_S^0 \pi^{\mp}$ phase-space position p, and $\delta(p)$ is the relative strong phase. The parameter κ accounts for the interference between $B^{\mp} \to \tilde{D}^0 K^{*\mp}$ and other $B^{\mp} \to \tilde{D}^0 K_S^0 \pi^{\mp}$ amplitudes with $0 < \kappa < 1$ in the most general case. This effective parametrization also accounts for efficiency variations as a function of the kinematics of the B decay.

In this paper we present an improved measurement of γ based on the analysis of the Dalitz plot distribution of $\tilde{D}^0 \to K_S^0 \pi^+ \pi^-$ and, for the first time, $\tilde{D}^0 \to K_S^0 K^+ K^-$, using a sample of 351 fb^{-1} of integrated luminosity recorded at the $\Upsilon(4S)$ resonance, corresponding to 383×10^6 $B\bar{B}$ pairs. We analyze a total of seven signal samples (also referred to as CP samples), $B^- \to \tilde{D}^{(*)0} K^-$ and $B^- \to \tilde{D}^0 K^{*-}$, with $\tilde{D}^{*0} \to \tilde{D}^0 \pi^0$, $\tilde{D}^0 \gamma$, $\tilde{D}^0 \to K_S^0 \pi^+ \pi^-$, $K_S^0 K^+ K^-$, and $K^{*-} \to K_S^0 \pi^-$ [5]. Because of the lack of statistics, the decay $B^- \to \tilde{D}^0 K^{*-}$ with $\tilde{D}^0 \to K_S^0 K^+ K^-$ has been excluded from the analysis. We also reconstruct high-statistics control samples, one for each signal B decay channel: $B^- \to D^{(*)0} \pi^-$ and (for $B^- \to \tilde{D}^0 K^{*-}$) $B^- \to D^0 a_1^-$ with $a_1^- \to \pi^- \pi^+ \pi^-$ [5,19]. We exploit the same data set to determine $\mathcal{A}_{D\mp}$ for $D^0 \to K_S^0 \pi^+ \pi^-$ and $D^0 \to K_S^0 K^+ K^-$ decays from analyses of the respective Dalitz plots for high-statistics samples of flavor-tagged D^0 mesons from $D^{*+} \to D^0 \pi^+$ decays [5], produced in $e^+ e^- \to c\bar{c}$ events. Additional improvements compared to our previous publication [18] include a higher reconstruction efficiency, an optimized treatment of the $e^+ e^- \to q\bar{q}$, $q = u$, d, s, c background and an improved $D^0 \to K_S^0 \pi^+ \pi^-$ description of the Dalitz plot distribution (referred to hereafter as the Dalitz model), resulting in a significant decrease of statistical, systematic, and model uncertainties. This measurement supersedes our previous result based on 227×10^6 $B\bar{B}$ pairs [18].

The paper is organized as follows. In Sec. II we describe the reconstruction and selection of the signal and control samples. Section III is devoted to the determination of $\mathcal{A}_{D\mp}$ for $D^0 \to K_S^0 \pi^+ \pi^-$ and $D^0 \to K_S^0 K^+ K^-$ decays. In Sec. IV we describe the simultaneous maximum likelihood fit to the distributions $\Gamma_-^{(*)}$ and $\Gamma_+^{(*)}$ for the $B^{\mp} \to \tilde{D}^{(*)0} K^{\mp}$ samples and to the analogous distributions for $B^{\mp} \to \tilde{D}^0 K^{*\mp}$, to determine the CP parameters $x_{\mp}^{(*)}$, $y_{\mp}^{(*)}$, $x_{s\mp}$, and $y_{s\mp}$. In that section we also present the experimental results, including systematic uncertainties. We extract these CP parameters since they have a good Gaussian behavior for small values of $r_B^{(*)}$, κr_s and relatively low statistics samples, independent of their values and precisions, in contrast to γ, $r_B^{(*)}$, $\delta_B^{(*)}$, κr_s, and δ_s. Finally, in

Sec. V, we interpret the experimental results and extract the physically relevant quantities γ, $r_B^{(*)}$, $\delta_B^{(*)}$, κr_s, and δ_s, using a statistical (frequentist) analysis.

II. EVENT SELECTION

A. *BABAR* detector

This analysis is based on a data sample collected by the *BABAR* detector at the Stanford Linear Accelerator Center PEP-II $e^+ e^-$ asymmetric-energy storage ring. The *BABAR* detector is described in detail elsewhere [20]. We summarize briefly the components that are crucial to this analysis. Charged-particle tracking is provided by a five-layer silicon vertex tracker (SVT) and a 40-layer drift chamber (DCH). In addition to providing precise space coordinates for tracking, the SVT and DCH also measure the specific ionization (dE/dx), which is used for particle identification of low-momentum charged particles. At higher momenta ($p > 0.7$ GeV/c) pions and kaons are identified by Cherenkov radiation detected in a ring-imaging device (DIRC). The typical separation between pions and kaons varies from 8σ at 2 GeV/c to 2.5σ at 4 GeV/c, where σ denotes here the standard deviation. The position and energy of photons are measured with an electromagnetic calorimeter consisting of 6580 thallium-doped CsI crystals. These systems are mounted inside a 1.5-T solenoidal superconducting magnet. We use a GEANT4-based Monte Carlo (MC) simulation to model the response of the detector, taking into account the varying accelerator and detector conditions, and to generate large samples of signal and background for the CP and control modes considered in the analysis.

B. Event reconstruction and selection

The B^- candidates are formed by combining a $\tilde{D}^{(*)0}$ candidate with a track identified as a negatively charged kaon [20] or with a K^{*-} candidate formed as a combination of a K_S^0 and a negatively charged pion, with an invariant mass within 55 MeV/c^2 of the nominal K^{*-} mass. Here and in the following, nominal mass values are taken from [21]. The $\tilde{D}^0$ candidates are selected by requiring the $K_S^0 \pi^+ \pi^-$ or $K_S^0 K^+ K^-$ invariant mass to be within 12 MeV/c^2 of the nominal D^0 mass, and the momentum in the center-of-mass (c.m.) frame to be greater than 1.3 GeV/c. The $K^{\mp}$ tracks in $\tilde{D}^0 \to K_S^0 K^+ K^-$ are required to be positively identified as kaons in the DCH and DIRC. The π^0 candidates from $\tilde{D}^{*0} \to \tilde{D}^0 \pi^0$ decays are formed from pairs of photons with invariant mass in the range [115, 150] MeV/c^2, and with photon energy greater than 30 MeV. Photon candidates from $\tilde{D}^{*0} \to \tilde{D}^0 \gamma$ decays are selected if their energy is greater than 100 MeV. The $\tilde{D}^0$ candidates are combined with a $\pi^0(\gamma)$ to form the $\tilde{D}^{*0}$ candidate, and are required to have a $\tilde{D}^{*0}$-$\tilde{D}^0$ mass difference within 2.5(10) MeV/c^2 of its nominal value. The K_S^0 candidates are reconstructed from pairs of oppositely

charged pions constrained to originate from the same point and with an invariant mass within 9 MeV/c^2 of the K_S^0 nominal mass. The cosine of the collinearity angle between the K_S^0 momentum and the line connecting its parent particle (the $\tilde{D}^0$ or the K^{*-}) and the K_S^0 decay points in the plane transverse to the beam is required to be larger than 0.990 (0.997 for K_S^0 from K^{*-} decays). This cut helps to significantly reduce background contributions from $\tilde{D}^0 \rightarrow \pi\pi\pi$ decays and from a_1^- misreconstructed as K^{*-}. The kinematic variables of the $\tilde{D}^{(*)0}$, K_S^0, and π^0 when forming the B^-, $\tilde{D}^0$, and $\tilde{D}^{*0}$, respectively, are fitted with masses constrained to nominal values. For $B^- \rightarrow \tilde{D}^0 K^{*-}$ decays we also require $|\cos\theta_H| \geq 0.35$, where θ_H is the angle between the momentum of the K^{*-} daughter pion and the parent B^- in the K^{*-} rest frame. The distribution of $\cos\theta_H$ is proportional to $\cos^2\theta_H$ for $B^- \rightarrow \tilde{D}^0 K^{*-}$ while it is approximately flat for $e^+ e^- \rightarrow q\bar{q}$, $q = u, d, s, c$ (continuum) background.

We characterize B mesons using two almost independent variables, the beam-energy substituted mass, $m_{ES} = \sqrt{(E_0^{*2}/2 + \mathbf{p}_0 \cdot \mathbf{p}_B)^2/E_0^2 - p_B^2}$, and the energy difference $\Delta E = E_B^* - E_0^*/2$, with $p = (E, \mathbf{p})$, where the subscripts 0 and B refer to the initial $e^+ e^-$ system and the B candidate, respectively, and the asterisk denotes the c.m. frame. The signal events peak at the B mass in m_{ES} and at zero in ΔE. The m_{ES} resolution is about 2.6 GeV/c^2 and does not depend on the decay mode or on the nature of the prompt particle (K^- or K^{*-} candidate). In contrast, the ΔE resolution depends on the momentum resolution of the $D^{(*)0}$ meson and the prompt particle, and ranges between 15 and 18 MeV, depending on the decay mode. We select events with $m_{ES} > 5.2$ GeV/c^2 and $-80 < \Delta E < 120$ MeV. We discriminate against the main background contribution coming from continuum events through the fit to the data, as described in Sec. II C.

For events in which multiple B candidates satisfy the selection criteria, the one whose measured $\tilde{D}^0$ mass differs from the nominal value by the least number of standard deviations, is accepted as a signal candidate. For $B^- \rightarrow \tilde{D}^0 K^{*-}$ decays we select the candidate with the smallest value for the sum of the squares of the differences from nominal values, in standard deviations, of both K^{*-} and $\tilde{D}^0$ masses. The fraction of events in which we reconstruct more than one candidate is less than 1% for $B^- \rightarrow \tilde{D}^{(*)0} K^-$ samples and about 6% for $B^- \rightarrow \tilde{D}^0 K^{*-}$. The cross feed among the different samples is negligible except for $B^- \rightarrow \tilde{D}^{*0}[\tilde{D}^0 \gamma] K^-$, where the background from $B^- \rightarrow \tilde{D}^{*0}[\tilde{D}^0 \pi^0] K^-$ is below 5% of the signal yield. If both $B^- \rightarrow \tilde{D}^{*0}[\tilde{D}^0 \pi^0] K^-$ and $B^- \rightarrow \tilde{D}^{*0}[\tilde{D}^0 \gamma] K^-$ candidates are selected in the same event, only the $B^- \rightarrow \tilde{D}^{*0}[\tilde{D}^0 \pi^0] K^-$ is kept. This contamination has a negligible effect on the measurement of the CP parameters.

Figure 2 shows the m_{ES} distributions in the ΔE signal region defined through the requirement $|\Delta E| < 30$ MeV,

after all selection criteria are applied. The reconstruction efficiencies are 20%, 9%, 12%, and 12%, for $B^- \rightarrow \tilde{D}^0 K^-$, $B^- \rightarrow \tilde{D}^{*0}[\tilde{D}^0 \pi^0] K^-$, $B^- \rightarrow \tilde{D}^{*0}[\tilde{D}^0 \gamma] K^-$, and $B^- \rightarrow \tilde{D}^0 K^{*-}$ decay modes, respectively, with $\tilde{D}^0 \rightarrow K_S^0 \pi^+ \pi^-$. Similarly, for $\tilde{D}^0 \rightarrow K_S^0 K^+ K^-$ channels we obtain 19%, 8%, and 11% ($B^- \rightarrow \tilde{D}^0 K^{*-}$ is not reconstructed).
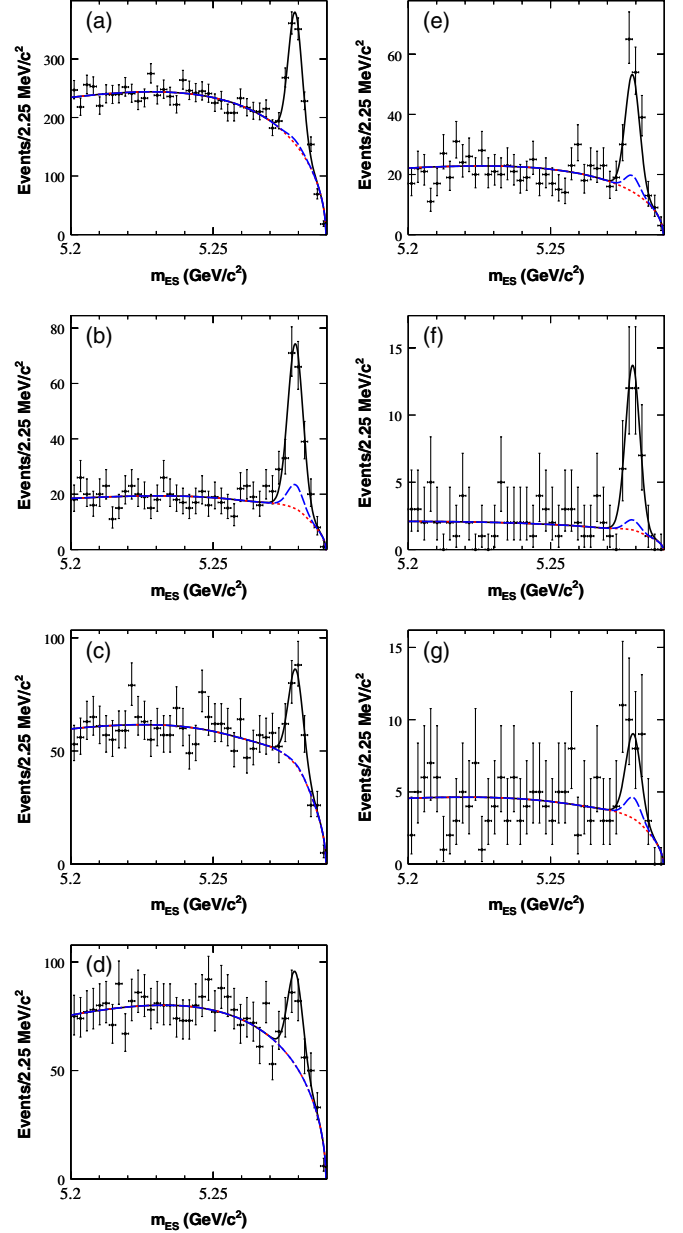
FIG. 2 (color online). Distributions of m_{ES} in ΔE signal region for (a), (e) $B^- \rightarrow \tilde{D}^0 K^-$, (b), (f) $B^- \rightarrow \tilde{D}^{*0}[\tilde{D}^0 \pi^0] K^-$, (c), (g) $B^- \rightarrow \tilde{D}^{*0}[\tilde{D}^0 \gamma] K^-$, and (d) $B^- \rightarrow \tilde{D}^0 K^{*-}$, with (a)–(d) $\tilde{D}^0 \rightarrow K_S^0 \pi^+ \pi^-$ and (e)–(g) $\tilde{D}^0 \rightarrow K_S^0 K^+ K^-$. The curves superimposed represent the projections of the fit described in Sec. II C: signal plus background (solid black lines), the continuum plus $B\bar{B}$ background contributions (dotted red lines), and the sum of the continuum, $B\bar{B}$, and K/π misidentification background components (dashed blue lines).

The same selection criteria are applied to select $B^- \to D^{(*)0}\pi^-$ control samples, apart from the particle identification requirement on the prompt track, which is replaced by a kaon identification veto. Since we evaluate ΔE with the kaon mass hypothesis, the ΔE distributions are shifted by approximately $+50$ MeV, as given by Eq. (4). $B^- \to D^0 a_1^-$ candidates are reconstructed similarly to $B^- \to \tilde{D}^0 K^{*-}$, with $a_1^- \to \rho(770)^0 \pi^-$ candidates made using combinations of three charged tracks with the requirements that the a_1^- invariant mass must be in the range $[1.0, 1.6]$ GeV/c^2, and that of the $\rho(770)^0$ within 150 MeV/c^2 of its nominal mass. As for signal samples, we select events with $-80 < \Delta E < 120$ MeV. Figure 3 shows the $m_{\rm ES}$ distributions for all control samples in the ΔE signal region defined through the requirement $20 < \Delta E < 80$ MeV, after all selection criteria. The corresponding reconstruction efficiencies are similar to those estimated for the CP samples.

C. Background composition and signal yields

The largest background contribution is from continuum events, where a fake or true $\tilde{D}^{(*)0}$ is combined with a random track ($B^- \to \tilde{D}^{(*)0} K^-$ samples), or a fake or true $\tilde{D}^0$ is combined with a random or fake K^* ($B^- \to \tilde{D}^0 K^{*-}$ sample). To separate continuum from $B\bar{B}$ events in a likelihood fit (discussed below and in Sec. IV), variables that characterize the event shape are used. We construct a Fisher discriminant $\mathcal{F}$ [22] from a linear combination of four topological variables: the monomials $L_0 = \sum_i p_i^*$ and $L_2 = \sum_i p_i^* |\cos\theta_i^*|^2$, $|\cos\theta_T^*|$, and $|\cos\theta_B^*|$. Here, p_i^* and θ_i^* are the c.m. momentum and the angle of the remaining tracks and clusters in the event, with respect to the B candidate thrust axis [23]. θ_T^* is the angle between the thrust axis of the B candidate and that of the rest of the event, and θ_B^* is the polar angle of the B candidate momentum, in the c.m. frame. The first three variables account for the jetlike shape of continuum events, in comparison to the spherical topology of $B\bar{B}$ events. In particular, the variable $|\cos\theta_T^*|$ peaks close to 1 for continuum while for $B\bar{B}$ it is essentially uniformly distributed. The angular distribution of the variable $|\cos\theta_B^*|$ follows $1 - \cos^2\theta_B^*$ for $B\bar{B}$ events and $1 + \cos^2\theta_B^*$ for $e^+ e^- \to q\bar{q}$ [24]. The strategy of using the Fisher discriminant in a likelihood fit enhances significantly, typically about 25%, the signal reconstruction efficiency compared to our previous analysis [18], where we required $|\cos\theta_T^*| < 0.8$. At the same time it provides a larger sample of continuum events in the $m_{\rm ES}$ sidebands, thus allowing the determination of the background properties directly from data (see Sec. IV).

Another source of background is related to $B\bar{B}$ decays where a fake or true $\tilde{D}^{(*)0}$ is combined with a random or misidentified track or K^*. The main single contribution for $B^- \to \tilde{D}^{(*)0} K^-$ signal comes from $B^- \to D^{(*)0}\pi^-$ decays
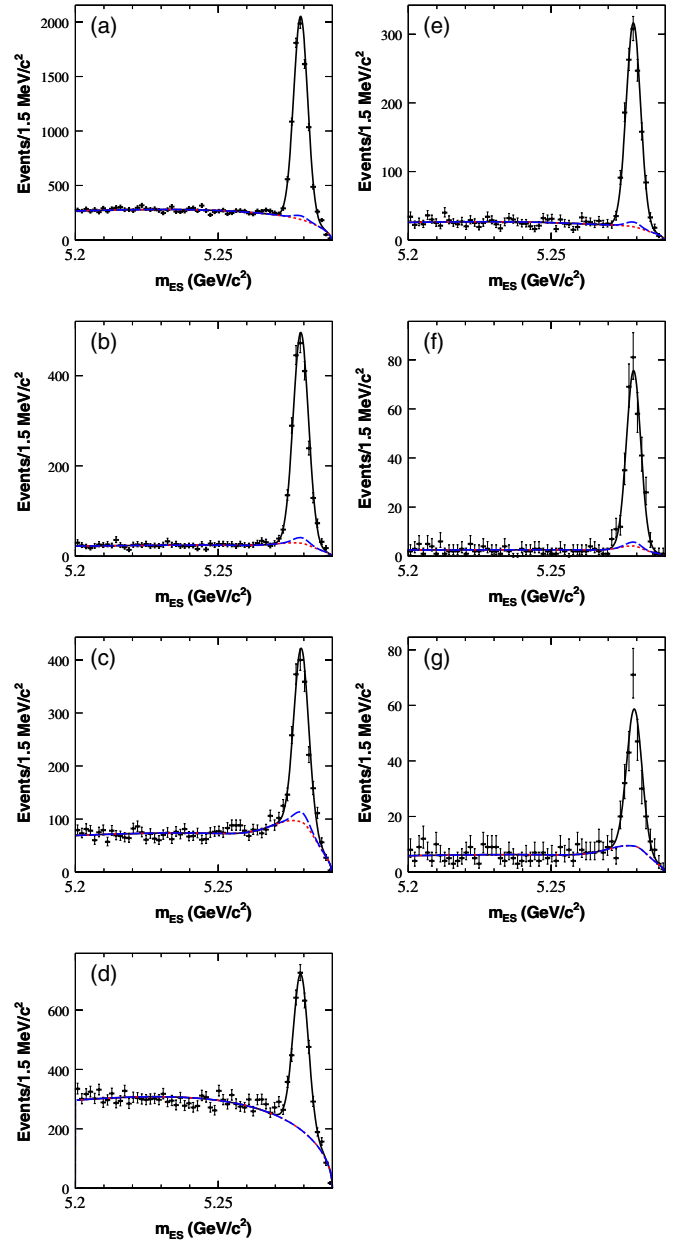
FIG. 3 (color online). Distributions of $m_{\rm ES}$ in ΔE signal region for (a), (e) $B^- \to \tilde{D}^0\pi^-$, (b), (f) $B^- \to \tilde{D}^{*0}[\tilde{D}^0\pi^0]\pi^-$, (c), (g) $B^- \to \tilde{D}^{*0}[\tilde{D}^0\gamma]\pi^-$, and (d) $B^- \to \tilde{D}^0 a_1^-$, with (a)–(d) $\tilde{D}^0 \to K_S^0 \pi^+ \pi^-$ and (e)–(g) $\tilde{D}^0 \to K_S^0 K^+ K^-$. The curves superimposed represent the projections of the fit described in Sec. II C: signal plus background (solid black lines), the continuum plus $B\bar{B}$ background contributions (dotted red lines), and the sum of the continuum, $B\bar{B}$, and K/π misidentification background components (dashed blue lines).

when the pion is misidentified as a kaon. This source is accounted for separately from other $B\bar{B}$ backgrounds. This contribution can be discriminated from the signal due to the shift in the ΔE distribution relative to that of signal events. Since ΔE is computed by assigning the kaon mass hypothesis to the prompt track, it is shifted by a quantity

$$\Delta E_{\text{shift}} = \gamma_{\text{PEP-II}}(\sqrt{m_K^2 + |\mathbf{p}|^2} - \sqrt{m_\pi^2 + |\mathbf{p}|^2}), \quad (4)$$

which depends on the momentum $\mathbf{p}$ of the prompt track in the laboratory frame and the Lorentz parameter $\gamma_{\text{PEP-II}}$ characterizing the boost of the c.m. relative to the laboratory frame, estimated from the PEP-II beam energies. For $B^- \to \tilde{D}^0 K^{*-}$ signal the main $B\bar{B}$ background source comes from $B^- \to D^0 a_1^-$ decays. Since this contribution is highly suppressed by the cut on the cosine of the collinearity angle at 0.997, it is not treated separately from other $B\bar{B}$ backgrounds. Non-K^* decays contributing to the $B^- \to \tilde{D}^0 K^{*-}$ sample are considered as signal, and their effect is accounted for by the factor κ defined in Eq. (3).

We fit the seven signal samples $B^- \to \tilde{D}^{(*)0} K^-$ and $B^- \to \tilde{D}^0 K^{*-}$, and their control samples $B^- \to D^{(*)0} \pi^-$ and $B^- \to D^0 a_1^-$, using an unbinned extended maximum likelihood method to extract signal and background yields, and probability density functions (PDFs) for the variables m_{ES}, ΔE, and the $\mathcal{F}$ discriminant, in the ΔE selection region. Three different background components are considered: continuum events, K/π misidentification (for $B^- \to \tilde{D}^{(*)0} K^-$ and $B^- \to D^{(*)0} \pi^-$ samples only), and other $\Upsilon(4S) \to B\bar{B}$ decays. The log likelihood for each of the CP and control samples is

$$\ln \mathcal{L} = -\eta + \sum_j \ln\left[\sum_c N_c \mathcal{P}_c(\mathbf{u}_j)\right], \quad (5)$$

where $\mathbf{u}_j = \{m_{\text{ES}}, \Delta E, \mathcal{F}\}_j$ characterizes the event j. Here, $\mathcal{P}_c(\mathbf{u}) = \mathcal{P}_c(m_{\text{ES}})\mathcal{P}_c(\Delta E)\mathcal{P}_c(\mathcal{F})$ is the combined selection PDF, verifying the normalization condition $\int \mathcal{P}_c(\mathbf{u})d\mathbf{u} = 1$, N_c the event yield for signal or background component c, and $\eta = \sum_c N_c$.

The signal m_{ES} distributions for each CP sample and its corresponding control sample are parametrized using a common single Gaussian. Similarly, the $\mathcal{F}$ PDF makes use of a double Gaussian with different widths for the left and right parts of the curve (bifurcated Gaussian), and is assumed common for all CP and control samples. The signal ΔE distribution for $B^- \to \tilde{D}^{(*)0} K^-$ events is parametrized with a double Gaussian function, while for $B^- \to D^{(*)0} \pi^-$ events we use the same function, shifted event by event using Eq. (4). For $B^- \to \tilde{D}^0 K^{*-}$ and $B^- \to \tilde{D}^0 a_1^-$ signal events a common double Gaussian is used instead.

The continuum background in the m_{ES} distribution is described by a threshold function [25] while the continuum ΔE distribution is described using a first order polynomial parametrization. The free parameters are different for each CP sample but common to the corresponding control sample. The $\mathcal{F}$ distribution for continuum background is parametrized with the sum of two Gaussian functions and assumed common for all samples.

The shape of the m_{ES} distribution for $\Upsilon(4S) \to B\bar{B}$ background (excluding the K/π misidentification contri-

bution, as indicated previously) is taken from generic $B\bar{B}$ simulated events for each CP and control sample independently, and uses a threshold function [25] to describe the combinatorial component plus a bifurcated Gaussian to parametrize the contribution peaking at the B mass. The fraction of the peaking contribution is extracted directly from the fit to the data, except for the $\tilde{D}^0 \to K_S^0 K^+ K^- CP$ samples, where it is taken from the generic $B\bar{B}$ MC due to lack of statistics. The ΔE distribution for $B\bar{B}$ background is taken similarly from simulation and is parametrized with the sum of a second order polynomial and an exponential function that takes into account the increase of combinatorial background at negative ΔE values. A Gaussian function is also included to account for a potential ΔE peaking background, although we find no significant peaking structure in any of our samples. The $\mathcal{F}$ distributions for signal and control samples, and for the generic $B\bar{B}$ background, are assumed to be the same as found in the simulation.

The selection fit yields, respectively, 610 ± 34, 156 ± 17, 114 ± 16, and 110 ± 15 signal candidates, for $B^- \to \tilde{D}^0 K^-$, $B^- \to \tilde{D}^{*0}[\tilde{D}^0 \pi^0] K^-$, $B^- \to \tilde{D}^{*0}[\tilde{D}^0 \gamma] K^-$, and $B^- \to \tilde{D}^0 K^{*-}$ reconstructed in the $\tilde{D}^0 \to K_S^0 \pi^+ \pi^-$ mode, in agreement with expectations based on measured branching fractions and efficiencies estimated from Monte Carlo simulation. Similarly, for $\tilde{D}^0 \to K_S^0 K^+ K^-$ channels we obtain, respectively, 132 ± 14, 35 ± 7, and 16 ± 6. The corresponding signal yields for control samples are 8262 ± 105, 2227 ± 55, 1446 ± 53, and 2321 ± 75, for $\tilde{D}^0 \to K_S^0 \pi^+ \pi^-$ decay modes, and 1402 ± 41, 350 ± 20, and 236 ± 20, for $\tilde{D}^0 \to K_S^0 K^+ K^-$. All errors are statistical only. The curves in Figs. 2 and 3 represent the fit projections on the m_{ES} variable, for the ΔE signal region.

III. $D^0 \to K_S^0 \pi^+ \pi^-$ AND $D^0 \to K_S^0 K^+ K^-$ AMPLITUDES

A. Selection of flavor-tagged D^0 mesons

The $D^0 \to K_S^0 \pi^+ \pi^-$ and $D^0 \to K_S^0 K^+ K^-$ (referred to hereafter collectively as $D^0 \to K_S^0 h^+ h^-$) decay amplitudes are determined from Dalitz plot analyses of D^0 mesons from $D^{*+} \to D^0 \pi^+$ decays produced in $e^+ e^- \to c\bar{c}$ events. The charge of the low-momentum π^+ from the D^{*+} decay identifies ("tags") the flavor of the D^0. Reconstruction and selection of $D^0 \to K_S^0 h^+ h^-$ candidates from $D^{*+} \to D^0 \pi^+$ decays are similar to those from $B^- \to \tilde{D}^{(*)0} K^-$ decays, the only exception being the kaon identification of only one charged kaon for $D^0 \to K_S^0 K^+ K^-$. The D^{*+} candidates are formed by combining the D^0 with the low-momentum charged track. The two D^{*+} decaying daughters are constrained to originate from the same point inside the PEP-II luminous region. To reduce combinatorial background and contamination from $B\bar{B}$ decays, the D^0 candidates are required to have a c.m. momentum greater than 2.2 GeV/c.

Each D^0 sample is characterized by the distributions of two variables, the invariant mass of the D^0 candidate m_D and the $\Delta m = D^{*+} - D^0$ mass difference. We select D^0 candidates within ± 0.64 and ± 0.61 MeV/c^2, corresponding to ± 2 standard deviations, around the nominal Δm [21], for $D^0 \to K_S^0 \pi^+ \pi^-$ and $D^0 \to K_S^0 K^+ K^-$, respectively. Figure 4 shows the resulting $D^0 \to K_S^0 h^+ h^-$ mass distributions. The m_D line shape is described using a two Gaussian function for the signal and a linear background, as also shown in Fig. 4. The m_D resolutions are 6.7 and 3.9 MeV/c^2, for $D^0 \to K_S^0 \pi^+ \pi^-$ and $D^0 \to K_S^0 K^+ K^-$. The mass resolution for the latter is better than that of the former because of the much smaller Q value involved. The signal purity in the signal box ($\pm 2\sigma$ cutoff on m_D, where σ stands for the m_D resolution) is 97.7% and 99.3%, with about 487 000 and 69 000 candidates, for $D^0 \to K_S^0 \pi^+ \pi^-$ and $D^0 \to K_S^0 K^+ K^-$. The Dalitz plot distributions for these events are shown in Fig. 5, with $m_\mp^2 = m_{K_S^0 h^\mp}^2$ and $m_0^2 = m_{h^+ h^-}^2$.

B. Dalitz plot analysis

Three-body charm decays are expected to proceed through intermediate quasi-two-body modes [26] and this is the observed pattern. We therefore use, as a baseline model to describe $\mathcal{A}_D(m_\mp^2, m_\pm^2)$, an isobar approach consisting of a coherent sum of two-body amplitudes (subscript r) and a "nonresonant" (subscript NR) contribution [27],

$$\mathcal{A}_D(\mathbf{m}) = \sum_r a_r e^{i\phi_r} \mathcal{A}_r(\mathbf{m}) + a_{NR} e^{i\phi_{NR}}, \quad (6)$$

where we have introduced the notation $\mathbf{m} \equiv (m_-^2, m_+^2)$. The parameters a_r (a_{NR}) and ϕ_r (ϕ_{NR}) are the magnitude and phase of the amplitude for component r (NR). The function $\mathcal{A}_r = F_D \times F_r \times T_r \times W_r$ is a Lorentz-invariant expression that describes the dynamic properties of the D^0 meson decaying into $K_S^0 h^+ h^-$ through an intermediate resonance r, as a function of position in the Dalitz plane. Here, F_D (F_r) is the Blatt-Weisskopf centrifugal barrier
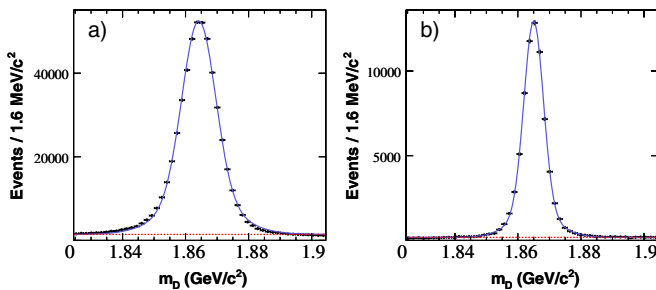
FIG. 4 (color online). D^0 mass distributions after all selection criteria, for (a) $D^{*+} \to D^0 \pi^+$, $D^0 \to K_S^0 \pi^+ \pi^-$ and (b) $D^{*+} \to D^0 \pi^+$, $D^0 \to K_S^0 K^+ K^-$. The curves superimposed represent the result from the m_D fit (solid blue lines) and the linear background contribution (dotted red lines).
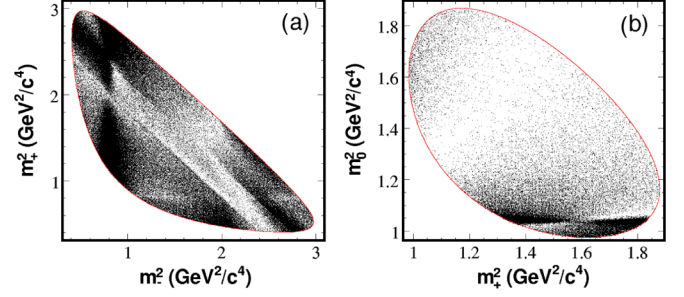
FIG. 5 (color online). Dalitz plot distributions for (a) $D^0 \to K_S^0 \pi^+ \pi^-$ and (b) $D^0 \to K_S^0 K^+ K^-$ from $D^{*+} \to D^0 \pi^+$ events after all selection criteria, in the D^0 mass signal region. The contours (solid red lines) represent the kinematical limits of the $D^0 \to K_S^0 \pi^+ \pi^-$ and $D^0 \to K_S^0 K^+ K^-$ decays.

factor for the D (resonance) decay vertex [28] with radius $R = 1.5$ GeV$^{-1} \hbar c \equiv 0.3$ fm, T_r is the resonance propagator, and W_r describes the angular distribution in the decay. For T_r we use a relativistic Breit-Wigner (BW) parametrization with mass-dependent width [27], except for $r = \rho(770)^0$ and $\rho(1450)^0$ resonances where we use the Gounaris-Sakurai functional form [29]. The angular dependence W_r is described using either Zemach tensors [30,31] where transversality is enforced or the helicity formalism [32–34] when we allow for a longitudinal component in the resonance propagator (see Ref. [27] for a comprehensive summary). Mass and width values are taken from [21], unless otherwise specified.

The complex $\pi\pi$ S-wave dynamics in the $D^0 \to K_S^0 \pi^+ \pi^-$ reaction [35], with the presence of several broad and overlapping scalar resonances, is more adequately described through the use of a K-matrix formalism [36] with the P-vector approximation [37]. This approach offers a direct way of imposing the unitarity constraint of the scattering matrix, not guaranteed in the case of the isobar model. The Dalitz plot amplitude $\mathcal{A}_D(\mathbf{m})$ given by Eq. (6) is then modified as

$$\mathcal{A}_D(\mathbf{m}) = F_1(s) + \sum_{r \neq (\pi\pi)_{L=0}} a_r e^{i\phi_r} \mathcal{A}_r(\mathbf{m}) + a_{NR} e^{i\phi_{NR}}, \quad (7)$$

where $F_1(s)$ is the contribution of $\pi\pi$ S-wave states written in terms of the K-matrix formalism,

$$F_u(s) = \sum_l [I - iK(s)\rho(s)]_{uv}^{-1} P_v(s). \quad (8)$$

Here, $s = m_0^2$ is the squared invariant mass of the $\pi^+ \pi^-$ system, I is the identity matrix, K is the matrix describing the S-wave scattering process, ρ is the phase-space matrix, and P is the initial production vector (P vector). The index u (and similarly v) represents the uth channel ($1 = \pi\pi$, $2 = K\bar{K}$, $3 = \pi\pi\pi\pi$, $4 = \eta\eta$, $5 = \eta\eta'$). In this framework, the production process can be viewed as the initial preparation of several states, which are then propagated by

the $[I - iK(s)\rho(s)]^{-1}$ term into the final one. The propagator can be described using scattering data, provided that the two-body system in the final state is isolated and does not interact with the rest of the final state in the production process. The P vector has to be determined from the data themselves since it depends on the production mechanism. Only the F_1 amplitude appears in Eq. (7) since we are describing the $\pi\pi$ channel. See Sec. III C for more details.

The decay amplitude $\mathcal{A}_D(\mathbf{m})$ is then determined from a maximum likelihood fit to the $D^0 \to K_S^0 h^+ h^-$ Dalitz plot distribution $\mathbf{m}$ in a $\pm 2\sigma$ cutoff region of the D^0 mass, with log-likelihood function

$$\ln\mathcal{L} = \sum_j \ln[f_{\text{sig}}\mathcal{D}_{\text{sig},\mp}(\mathbf{m}_j) + (1 - f_{\text{sig}})\mathcal{D}_{\text{bkg},\mp}(\mathbf{m}_j)],$$
$$(9)$$

where f_{sig} represents the fraction of signal obtained from the fit to the mass spectrum, and $\mathcal{D}_{\text{sig(bkg)},\mp}(\mathbf{m}_j)$ is the signal (background) Dalitz plot PDF for event j, satisfying the condition $\int \mathcal{D}_{\text{sig(bkg)},\mp}(\mathbf{m})d\mathbf{m} = 1$. For D^0 signal events, $\mathcal{D}_{\text{sig},+}(\mathbf{m}) = |\mathcal{A}_D(\mathbf{m})|^2\epsilon(\mathbf{m})$, while for $\bar{D}^0$, $\mathcal{D}_{\text{sig},-}(\mathbf{m}) = |\mathcal{A}_D(\bar{\mathbf{m}})|^2\epsilon(\mathbf{m})$, with $\bar{\mathbf{m}} \equiv (m_+^2, m_-^2)$. Here $\epsilon(\mathbf{m})$ represents the efficiency variations on the Dalitz plot, evaluated using high-statistics signal MC samples. These are generated according to a uniform distribution and parametrized using third-order polynomial functions in two dimensions, symmetric for $D^0 \to K_S^0\pi^+\pi^-$ and asymmetric for $D^0 \to K_S^0 K^+ K^-$ to account for possible charge asymmetries in the K^- and K^+ detection efficiencies. The Dalitz plot distributions for the background, $\mathcal{D}_{\text{bkg},\mp}(\mathbf{m})$, are determined using D^0 mass sideband data.

For each contribution r we evaluate the fit fraction as the normalized integral of $a_r^2|\mathcal{A}_r(\mathbf{m})|^2$ over the Dalitz plane [27],

$$f_r = \frac{a_r^2 \int |\mathcal{A}_r(\mathbf{m})|^2 d\mathbf{m}}{\sum_r \sum_{r'} a_r a_{r'}^* \int \mathcal{A}_r(\mathbf{m})\mathcal{A}_{r'}^*(\mathbf{m})d\mathbf{m}}. \qquad (10)$$

The sum of fit fractions does not necessarily add up to unity because of interference effects among the amplitudes.

C. $D^0 \to K_S^0 \pi^+ \pi^-$ Dalitz model

The P and D waves of the $D^0 \to K_S^0\pi^+\pi^-$ decay amplitude are described using a total of six resonances leading to eight two-body decay amplitudes: the Cabibbo allowed (CA) $K^*(892)^-$, $K^*(1680)^-$, $K_2^*(1430)^-$, the doubly Cabibbo suppressed (DCS) $K^*(892)^+$, $K_2^*(1430)^+$, and the CP eigenstates $\rho(770)^0$, $\omega(782)$, and $f_2(1270)$. Since the $K\pi$ P wave is largely dominated by the $K^*(892)^{\mp}$, the mass and width of this resonance are simultaneously determined from our fit to the tagged D^0 sample, $M_{K^*(892)^{\mp}} = 893.61 \pm 0.08$ MeV$/c^2$ and $\Gamma_{K^*(892)^{\mp}} = 46.34 \pm 0.16$ MeV$/c^2$ (errors are statistical only). The mass and width values of the $K^*(1680)^-$ are taken from [38], where the interference between the $K\pi$ S and P waves is properly accounted for.

We adopt the same parametrizations for K, ρ, and P in Eq. (8) as in Refs. [27,39,40]. For the K matrix we have

$$K_{uv}(s) = \left(\sum_\alpha \frac{g_u^\alpha g_v^\alpha}{m_\alpha^2 - s} + f_{uv}^{\text{scatt}}\frac{1 - s_0^{\text{scatt}}}{s - s_0^{\text{scatt}}}\right)f_{A0}(s), \quad (11)$$

where g_u^α is the coupling constant of the K-matrix pole m_α to the uth channel. The parameters f_{uv}^{scatt} and s_0^{scatt} describe the slowly varying part of the K matrix. The factor

$$f_{A0}(s) = \frac{1 - s_{A0}}{s - s_{A0}}\left(s - s_A\frac{m_\pi^2}{2}\right), \qquad (12)$$

suppresses the false kinematical singularity at $s = 0$ in the physical region near the $\pi\pi$ threshold (the Adler zero [41]). The parameter values used in this analysis are listed in Table I and are obtained from a global analysis of the available $\pi\pi$ scattering data from threshold up to 1900 MeV$/c^2$ [39]. The parameters f_{uv}^{scatt}, for $u \neq 1$, are all set to zero since they are not related to the $\pi\pi$ scattering process. Similarly, for the P vector we have

TABLE I. K-matrix parameters from a global analysis of the available $\pi\pi$ scattering data from threshold up to 1900 MeV$/c^2$ [39]. Masses and coupling constants are given in GeV$/c^2$.

m_α	$g_{\pi^+\pi^-}^\alpha$	$g_{K\bar{K}}^\alpha$	$g_{4\pi}^\alpha$	$g_{\eta\eta}^\alpha$	$g_{\eta\eta'}^\alpha$
0.651 00	0.228 89	−0.553 77	0.000 00	−0.398 99	−0.346 39
1.203 60	0.941 28	0.550 95	0.000 00	0.390 65	0.315 03
1.558 17	0.368 56	0.238 88	0.556 39	0.183 40	0.186 81
1.210 00	0.336 50	0.409 07	0.856 79	0.199 06	−0.009 84
1.822 06	0.181 71	−0.175 58	−0.796 58	−0.003 55	0.223 58
s_0^{scatt}	f_{11}^{scatt}	f_{12}^{scatt}	f_{13}^{scatt}	f_{14}^{scatt}	f_{15}^{scatt}
−3.926 37	0.233 99	0.150 44	−0.205 45	0.328 25	0.354 12
s_{A0}	s_A				
−0.15	1				

$$P_v(s) = \sum_\alpha \frac{\beta_\alpha g_v^\alpha}{m_\alpha^2 - s} + f_{1v}^{\text{prod}} \frac{1 - s_0^{\text{prod}}}{s - s_0^{\text{prod}}}. \quad (13)$$

Note that the P vector has the same poles as the K matrix; otherwise the F_1 vector would vanish (diverge) at the K matrix (P vector) poles. The parameters β_α, f_{1v}^{prod}, and s_0^{prod} of the initial P vector are obtained from our fit to the tagged $D^0 \to K_S^0 \pi^+ \pi^-$ data sample.

For the $K\pi$ S-wave contribution to Eq. (7) we use a parametrization extracted from scattering data [38] which consists of a $K_0^*(1430)^-$ or $K_0^*(1430)^+$ BW (for CA or DCS contribution, respectively) together with an effective range nonresonant component with a phase shift,

$$\mathcal{A}_{K\pi L=0}(\mathbf{m}) = F \sin\delta_F e^{i\delta_F} + R \sin\delta_R e^{i\delta_R} e^{i2\delta_F}, \quad (14)$$

with

$$\delta_R = \phi_R + \tan^{-1}\left[\frac{M\Gamma(m_{K\pi}^2)}{M^2 - m_{K\pi}^2}\right],$$
$$\delta_F = \phi_F + \cot^{-1}\left[\frac{1}{aq} + \frac{rq}{2}\right]. \quad (15)$$

The parameters a and r play the role of a scattering length and effective interaction length, respectively, F (ϕ_F) and R (ϕ_R) are the amplitudes (phases) for the nonresonant and resonant terms, and q is the momentum of the spectator particle in the $K\pi$ system rest frame. Note that the phases δ_F and δ_R depend on $m_{K\pi}^2$. M and $\Gamma(m_{K\pi}^2)$ are the mass and running width of the resonant term. This parametrization corresponds to a K-matrix approach describing a rapid phase shift coming from the resonant term and a slow rising phase shift governed by the nonresonant term, with relative strengths R and F [42]. The parameters M, Γ, F, ϕ_F, R, ϕ_R, a, and r are determined from our fit to the tagged D^0 sample, along with the other parameters of the model. Other recent experimental efforts to improve the description of the $K\pi$ S wave using K-matrix and model independent parametrizations from high-statistics samples of $D^+ \to K^- \pi^+ \pi^+$ decays are described in Ref. [43].

Table II summarizes the values obtained for all free parameters of the $D^0 \to K_S^0 \pi^+ \pi^-$ Dalitz model: CA, DCS, and CP eigenstates complex amplitudes $a_r e^{i\phi_r}$, $\pi^+ \pi^-$ S-wave P-vector parameters, and $K\pi$ S-wave parameters, along with the fit fractions. The nonresonant term of Eq. (7) has not been included since the $\pi\pi$ and $K\pi$ S-wave parametrizations naturally account for their respective nonresonant contributions. The fifth P-vector channel and pole have also been excluded since the $\eta\eta'$ threshold and the pole mass m_5 are both far beyond our $\pi\pi$ kinematic range, and thus there is little sensitivity to the associated parameters, f_{15}^{prod} and β_5, respectively. The amplitudes are measured with respect to $D^0 \to K_S^0 \rho(770)^0$ which gives the second largest contribution. We report statistical errors only for the amplitudes, but for the fit fractions we also include systematic uncertainties (see

Sec. III E), which largely dominate. The $K\pi$ and $\pi\pi$ P waves dominate the decay, but significant contributions from the corresponding S waves are also observed (above 6 and 4 standard deviations, respectively). We obtain a sum of fit fractions of $(103.6 \pm 5.2)\%$, and the goodness of fit is estimated through a two-dimensional χ^2 test performed binning the Dalitz plot into square regions of size $0.015 \text{ GeV}^2/c^4$, yielding a reduced χ^2 of 1.11 (including statistical errors only) for 19 274 degrees of freedom. The variation of the contribution to the χ^2 as a function of the Dalitz plot position is approximately uniform. Figures 6 (a)–6(c) show the Dalitz fit projections overlaid with the data distributions. The Dalitz plot distributions are well reproduced, with some small discrepancies in low and high mass regions of the m_0^2 projection, and in the $\rho(770)^0 - \omega(782)$ interference region.

As a cross-check, we alternatively parametrize the $\pi\pi$ and $K\pi$ S waves using the isobar approximation with the following BW amplitudes (plus the nonresonant contribution): the CA $K_0^*(1430)^-$, the DCS $K_0^*(1430)^+$, and the CP eigenstates $f_0(980)$, $f_0(1370)$, σ and an *ad hoc* σ'. This model is very similar to that used in our previous measurement of γ [18], except that the $K^*(1410)^-$ and $\rho(1450)^0$ resonances have been removed because of their negligible fit fractions. Masses and widths of the σ and σ' scalars are obtained from the fit, $M_\sigma = 528 \pm 5$, $\Gamma_\sigma = 512 \pm 9$, $M_{\sigma'} = 1033 \pm 4$, and $\Gamma_{\sigma'} = 99 \pm 6$, given in MeV/$c^2$. Mass and width values for the $K_0^*(1430)^\mp$, $f_0(980)$, and $f_0(1370)$ are taken from [44,45]. We obtain a sum of fit fractions of 122.5%, and a reduced χ^2 of 1.20 (with statistical errors only) for 19,274 degrees of freedom, which strongly disfavors the isobar approach in comparison to the K-matrix formalism.

D. $D^0 \to K_S^0 K^+ K^-$ Dalitz model

The description of the $D^0 \to K_S^0 K^+ K^-$ decay amplitude uses Eq. (6) and consists of five distinct resonances leading to eight two-body decays: $K_S^0 a_0(980)^0$, $K_S^0 \phi(1020)$, $K^- a_0(980)^+$, $K_S^0 f_0(1370)$, $K^+ a_0(980)^-$, $K_S^0 f_2(1270)^0$, $K_S^0 a_0(1450)^0$, and $K^- a_0(1450)^+$. This isobar model is essentially identical to that used in our previous analysis of the same reaction [46], but for the addition of the $a_0(1450)$ scalar, whose contribution is strongly supported by the much larger data sample, as well as of a D-wave contribution parametrized with the $f_2(1270)$ tensor. Attempts to improve the model quality by adding other contributions (including the nonresonant term) did not give better results.

The $\phi(1020)$ resonance is described using a relativistic BW, with mass and width left free in our fit to the D^0 tagged sample in order to account for mass resolution effects. The $a_0(980)$ resonance has a mass very close to the $K\bar{K}$ threshold and decays mostly to $\eta\pi$. Therefore it is described using a coupled channel BW [27,46], where the mass pole and coupling constant to $\eta\pi$ are taken from [47],

TABLE II.   CA, DCS, and *CP* eigenstates complex amplitudes $a_r e^{i\phi_r}$, $\pi\pi$ *S*-wave *P*-vector parameters, $K\pi$ *S*-wave parameters, and fit fractions, as obtained from the fit of the $D^0 \to K_S^0 \pi^+ \pi^-$ Dalitz plot distribution from $D^{*+} \to D^0 \pi^+$. *P*-vector parameters $f_{1\nu}^{\prime \mathrm{prod}}$, for $\nu \neq 1$, are defined as $f_{1\nu}^{\mathrm{prod}}/f_{11}^{\mathrm{prod}}$. Errors for amplitudes are statistical only, while for fit fractions include statistical and systematic uncertainties, largely dominated by the latter. Upper limits on fit fractions are quoted at 95% confidence level.

Component	a_r	ϕ_r (deg)	Fraction (%)
$K^*(892)^-$	1.740 ± 0.010	139.0 ± 0.3	55.7 ± 2.8
$K_0^*(1430)^-$	8.2 ± 0.7	153 ± 8	10.2 ± 1.5
$K_2^*(1430)^-$	1.410 ± 0.022	138.4 ± 1.0	2.2 ± 1.6
$K^*(1680)^-$	1.46 ± 0.10	-174 ± 4	0.7 ± 1.9
$K^*(892)^+$	0.158 ± 0.003	-42.7 ± 1.2	0.46 ± 0.23
$K_0^*(1430)^+$	0.32 ± 0.06	143 ± 11	<0.05
$K_2^*(1430)^+$	0.091 ± 0.016	85 ± 11	<0.12
$\rho(770)^0$	1	0	21.0 ± 1.6
$\omega(782)$	0.0527 ± 0.0007	126.5 ± 0.9	0.9 ± 1.0
$f_2(1270)$	0.606 ± 0.026	157.4 ± 2.2	0.6 ± 0.7
β_1	9.3 ± 0.4	-78.7 ± 1.6	
β_2	10.89 ± 0.26	-159.1 ± 2.6	
β_3	24.2 ± 2.0	168 ± 4	
β_4	9.16 ± 0.24	90.5 ± 2.6	
f_{11}^{prod}	7.94 ± 0.26	73.9 ± 1.1	
$f_{12}^{\prime \mathrm{prod}}$	2.0 ± 0.3	-18 ± 9	
$f_{13}^{\prime \mathrm{prod}}$	5.1 ± 0.3	33 ± 3	
$f_{14}^{\prime \mathrm{prod}}$	3.23 ± 0.18	4.8 ± 2.5	
s_0^{prod}	-0.07 ± 0.03		
$\pi\pi$ *S* wave			11.9 ± 2.6
M (GeV/c^2)	1.463 ± 0.002		
Γ (GeV/c^2)	0.233 ± 0.005		
F	0.80 ± 0.09		
ϕ_F	2.33 ± 0.13		
R	1		
ϕ_R	-5.31 ± 0.04		
a	1.07 ± 0.11		
r	-1.8 ± 0.3		
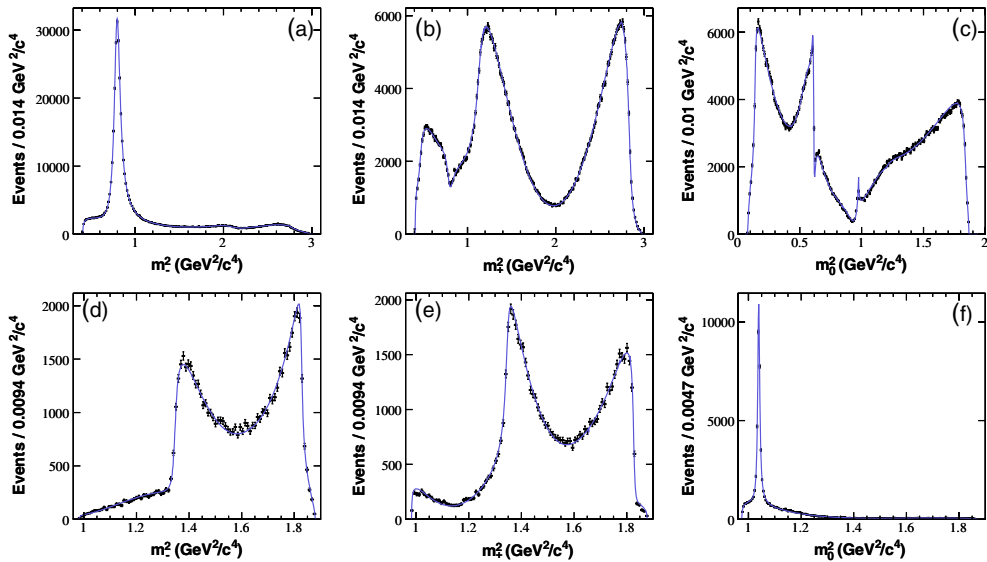
FIG. 6 (color online). $D^0 \to K_S^0 h^+ h^-$ Dalitz plot projections from $D^{*+} \to D^0 \pi^+$ events on (a), (d) m_-^2, (b), (e) m_+^2, and (c), (f) m_0^2, for (a)–(c) $D^0 \to K_S^0 \pi^+ \pi^-$ and (d)–(f) $D^0 \to K_S^0 K^+ K^-$. The curves are the reference model fit projections.

while the coupling constant to $K\bar{K}$, $g_{K\bar{K}}$, is determined from our fit.

Table III summarizes the values obtained for all free parameters of the $D^0 \rightarrow K_S^0 K^+ K^-$ Dalitz model, the complex amplitudes $a_r e^{i\phi_r}$, the mass and width of the $\phi(1020)$ and the coupling constant $g_{K\bar{K}}$, together with the fit fractions. The value of $g_{K\bar{K}}$ is consistent with our previous result [46], and differs significantly from the measurement reported in [47]. All amplitudes are measured with respect to $D^0 \rightarrow K_S^0 a_0(980)^0$, which gives the largest contribution. The sum of fit fractions is 152.3%, and the reduced χ^2 is 1.09 (with statistical errors only) for 6856 degrees of freedom, estimated from a binning of the Dalitz plot into square regions of size 0.045 GeV^2/c^4. The variation of the contribution to the χ^2 as a function of the Dalitz plot position is approximately uniform in the regions where most of the decay dynamics occurs. Figures 6(d)–6(f) show the fit projections overlaid with the data distributions. The Dalitz plot distributions are well reproduced, with some small discrepancies at the peaks of the m_-^2 and m_+^2 projections.

E. Systematic uncertainties

Systematic uncertainties on $\mathcal{A}_D(\mathbf{m})$ are evaluated by repeating the fit to the tagged D^0 samples with alternative assumptions to those adopted in the reference $D^0 \rightarrow K_S^0 \pi^+ \pi^-$ and $D^0 \rightarrow K_S^0 K^+ K^-$ amplitude analyses. These uncertainties can then be directly propagated to the measurement of the CP parameters, as discussed in Sec. IV B, and the total systematic error can be obtained from the sum square of the individual contributions. In this paper we have also propagated these systematic uncertainties to the measurement of the $D^0 \rightarrow K_S^0 \pi^+ \pi^-$ fit fractions, as reported in Table II. In general, each of the considered alternative models has a reduced χ^2 poorer than that of the reference. Therefore, our systematic uncertainties do not include potential contributions due to the residual poor quality of the reference model fit, as reported in Secs. III C and III D.

1. Model contributions

Dalitz model systematic uncertainties on $\mathcal{A}_D(\mathbf{m})$ are related to the model dependence of the strong charm decay phase as a function of the Dalitz plot position when it is determined from the Dalitz plot density, which only depends on decay rates.

We use alternative models where the BW parameters are varied according to their uncertainties or changed by values measured by other experiments. This is the case of the $f_0(1370)$, where the reference values [44] are replaced by alternative measurements [48], and the $K^*(1680)^-$, where the reference parameters [38] are replaced by those from [21]. We also build models using alternative parametrizations, as in the case of the $\rho(770)^0$ where the reference Gounaris-Sakurai form is replaced by the standard relativistic BW.

To estimate the $\pi\pi$ S-wave systematic error we replace the reference K-matrix solution (Table I) by all alternative solutions analyzed in Ref. [39]. Analogously, the uncertainty on the parametrization of the $K\pi$ S wave is estimated using a standard relativistic BW describing the $K_0^*(1430)^{\mp}$ with parameters taken either from [44] or simultaneously determined from our fit to the D^0 sample. Additionally, the isobar model is used as a cross-check of the combined $\pi\pi$ and $K\pi$ S-wave effects.

Uncertainties due to our choice of the angular dependence are estimated by replacing the reference Zemach tensors by the helicity formalism. The effect is negligible for S waves, very small for P waves, but larger for D waves [31]. Other alternative models are built by changing the Blatt-Weisskopf radius between 0 and 3 $\text{GeV}^{-1}\hbar c$, and removing and adding resonances with small or negligible fit fractions. For $D^0 \rightarrow K_S^0 \pi^+ \pi^-$, we added $\rho(1450)^0$ and CA $K^*(1410)^-$. Similarly, for $D^0 \rightarrow K_S^0 K^+ K^-$, we removed all the $a_0(1450)$ states and the $f_2(1270)$, and added the $f_0(980)$ and the charged DCS $a_0(1450)$. The $f_0(980)$ resonance is described using a coupled channel BW with parameters taken from a variety of experiments [45,48,49].

2. Experimental contributions

Experimental systematic errors come from uncertainties in the knowledge of variations of the reconstruction efficiency on the Dalitz plot, background Dalitz plot shapes, mass resolution, mistag rate, and binning.

The uncertainty from the efficiency variations on the Dalitz plot $\epsilon(\mathbf{m})$ has been evaluated assuming the efficiency to be flat. Tracking efficiency studies in data and MC show that this method gives a conservative estimate of

TABLE III. *CP* eigenstates, CA, and DCS complex amplitudes $a_r e^{i\phi_r}$ and fit fractions, obtained from the fit of the $D^0 \rightarrow K_S^0 K^+ K^-$ Dalitz plot distribution from $D^{*+} \rightarrow D^0 \pi^+$. The mass and width of the $\phi(1020)$, and the $g_{K\bar{K}}$ coupling constant are simultaneously determined in the fit, yielding $M_{\phi(1020)} = 1.019\,43 \pm 0.000\,02$ GeV/c^2, $\Gamma_{\phi(1020)} = 4.593\,19 \pm 0.000\,04$ MeV/c^2, and $g_{K\bar{K}} = 0.550 \pm 0.010$ GeV/c^2. Errors are statistical only. Uncertainties (largely dominated by systematic contributions) are not estimated for the fit fractions.

Component	a_r	ϕ_r (deg)	Fraction (%)
$K_S^0 a_0(980)^0$	1	0	55.8
$K_S^0 \phi(1020)$	0.227 ± 0.005	-56.2 ± 1.0	44.9
$K_S^0 f_0(1370)$	0.04 ± 0.06	-2 ± 80	0.1
$K_S^0 f_2(1270)$	0.261 ± 0.020	-9 ± 6	0.3
$K_S^0 a_0(1450)^0$	0.65 ± 0.09	-95 ± 10	12.6
$K^- a_0(980)^+$	0.562 ± 0.015	179 ± 3	16.0
$K^- a_0(1450)^+$	0.84 ± 0.04	97 ± 4	21.8
$K^+ a_0(980)^-$	0.118 ± 0.015	138 ± 7	0.7

the imperfections of the detector simulation, which appear mainly at the boundaries of the phase space because of the presence of very low-momentum tracks.

Systematic errors related to the background Dalitz plot profile $\mathcal{D}_{\text{bkg},\mp}(\mathbf{m})$ are determined assuming a flat shape, which gives the largest effect among other alternative profiles obtained using either the m_D sideband from continuum MC, or the m_D signal region from continuum MC after removal of true D^0 mesons.

All the resonances, except for the $\omega(782)$ and $\phi(1020)$, have intrinsic width significantly larger than possible bias on invariant mass measurement and resolution. We estimate the systematic uncertainty associated with $\omega(782)$ by repeating the model fit using an overall width resulting from adding in quadrature its natural width and the mass resolution in the 782 MeV/c^2 $\pi\pi$ mass region. No systematic error is assigned for the $\phi(1020)$, since the reference model has been extracted with its mass and width as free parameters.

The uncertainty due to a wrong identification of the flavor of the D^0 ($\bar{D}^0$) meson from the $D^{*+} \to D^0\pi^+$ ($D^{*-} \to \bar{D}^0\pi^-$) decay, due to the association of the D meson with a random soft pion of incorrect charge has been evaluated taking into account explicitly the rate of mistags observed in the MC, at 0.7% level.

Effects from limited numerical precision in the computation of normalization integrals and binning in the Dalitz plane have been evaluated using coarser and thinner bins.

IV. DALITZ PLOT ANALYSIS OF $B^- \to D^{(*)}K^-$ AND $B^- \to DK^{*-}$ DECAYS

Once the decay amplitudes $\mathcal{A}_D(\mathbf{m})$ for $D^0 \to K_S^0\pi^+\pi^-$ and $D^0 \to K_S^0K^+K^-$ are known, they are fed into $\Gamma_{\mp}^{(*)}(\mathbf{m})$ and $\Gamma_{s\mp}(\mathbf{m})$. The extraction of the *CP*-violating parameters $x_{\mp}^{(*)}$, $y_{\mp}^{(*)}$, $x_{s\mp}$, and $y_{s\mp}$ is then performed through a simultaneous unbinned maximum likelihood fit (referred to hereafter as the *CP* fit) to the $\Gamma_{\mp}^{(*)}(\mathbf{m})$ and $\Gamma_{s\mp}(\mathbf{m})$ Dalitz plot distributions of the seven signal modes, in the ΔE signal region defined as $|\Delta E| < 30$ MeV. Figures 7 and 8 show these distributions separately for B^- and B^+ decays in a region enriched in signal through the requirements $m_{ES} > 5.272$ GeV/c^2 and $\mathcal{F} > -0.1$. The efficiency of the Fisher cut in the $|\Delta E| < 30$ MeV and $m_{ES} > 5.272$ GeV/c^2 region is around 70% for signal events, while for continuum background events it is below 1%.

The log-likelihood function for each of the seven *CP* samples generalizes Eq. (5) to include the Dalitz plot distributions,

$$\ln\mathcal{L} = -\eta + \sum_j \ln\left[\sum_c \frac{N_c}{2}(1 \pm A_c)\mathcal{P}_c(\mathbf{u}_j)\mathcal{D}_{c,\mp}(\mathbf{m}_j)\right].$$

(16)

Here, $\mathcal{D}_{c,\mp}(\mathbf{m}_j)$ is the Dalitz plot PDF for event j satisfying the normalization condition $\int \mathcal{D}_{c,\mp}(\mathbf{m})d\mathbf{m} = 1$, and
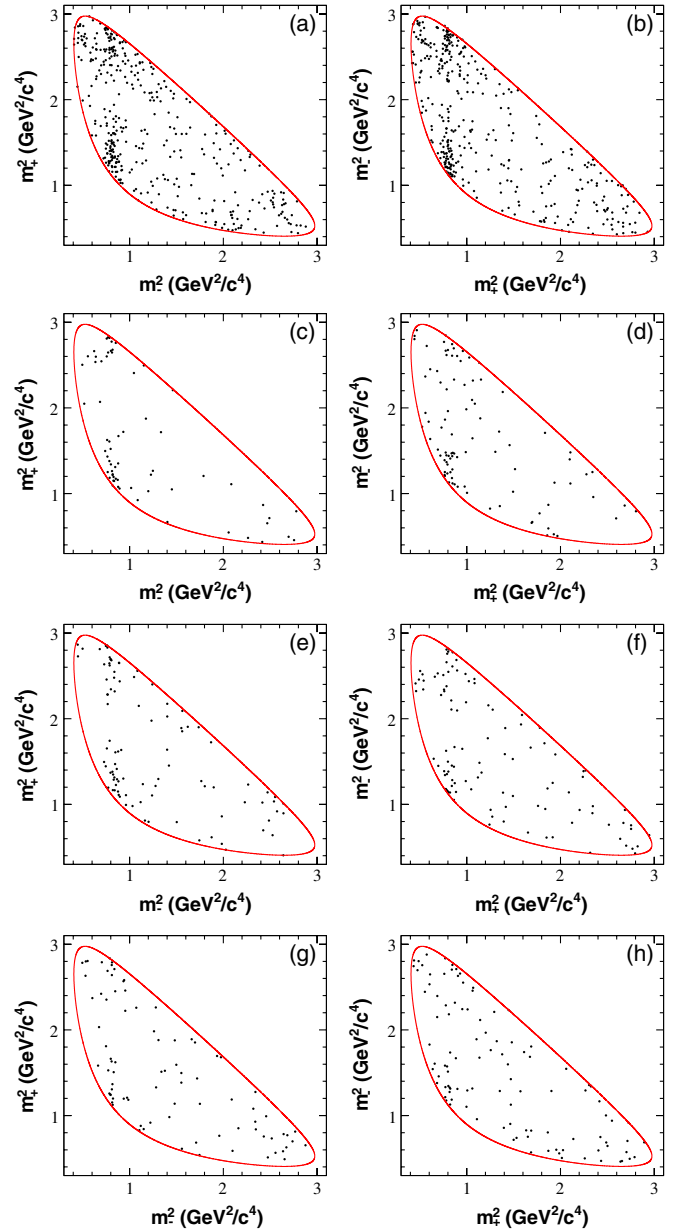
FIG. 7 (color online). $\tilde{D}^0 \to K_S^0\pi^+\pi^-$ Dalitz plot distributions for (a) $B^- \to \tilde{D}^0K^-$, (b) $B^+ \to \tilde{D}^0K^+$, (c) $B^- \to \tilde{D}^{*0}[\tilde{D}^0\pi^0]K^-$, (d) $B^+ \to \tilde{D}^{*0}[\tilde{D}^0\pi^0]K^+$, (e) $B^- \to \tilde{D}^{*0}[\tilde{D}^0\gamma]K^-$, (f) $B^+ \to \tilde{D}^{*0}[\tilde{D}^0\gamma]K^+$, (g) $B^- \to \tilde{D}^0K^{*-}$, and (h) $B^+ \to \tilde{D}^0K^{*+}$, for the ΔE signal region. The requirements $m_{ES} > 5.272$ GeV/c^2 and $\mathcal{F} > -0.1$ have been applied to reduce the background contamination, mainly from continuum events. The contours (solid red lines) represent the kinematical limits of the $\tilde{D}^0 \to K_S^0\pi^+\pi^-$ decay.

A_c accounts for any asymmetry in the absolute number of B^- and B^+ candidates (charge asymmetry) for component c.

For the $B^{\mp} \to \tilde{D}^0K^{\mp}$ signal, $\mathcal{D}_{\text{sig},\mp}(\mathbf{m}) = \Gamma_{\mp}(\mathbf{m})\epsilon(\mathbf{m})$, where the efficiency map in the Dalitz plot $\epsilon(\mathbf{m})$ is determined as for $D^{*+} \to D^0\pi^+$ events (Sec. III B). We replace r_B^2 in Eq. (2) by $r_{B^{\mp}}^2 = x_{\mp}^2 + y_{\mp}^2$. The physical condition
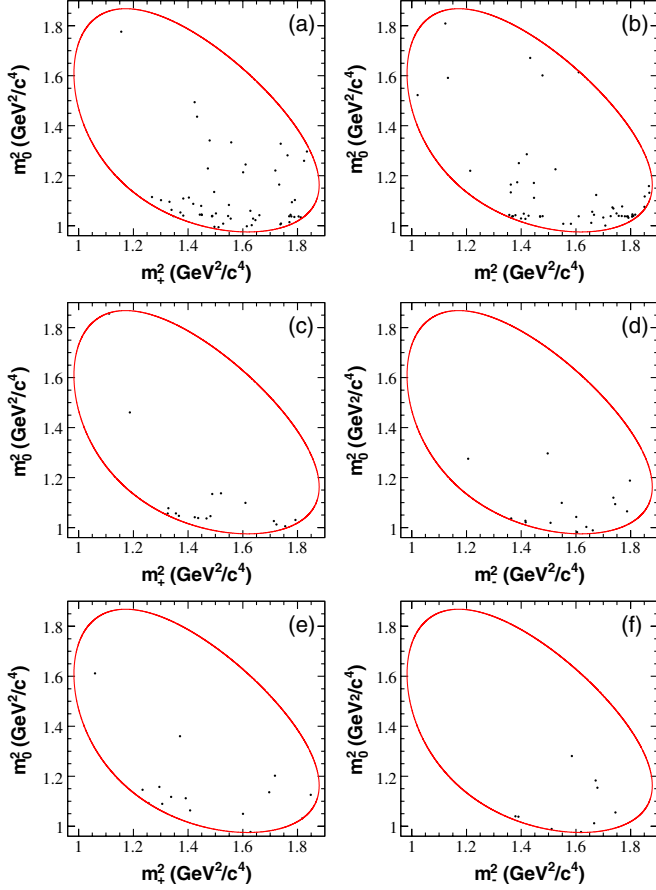
FIG. 8 (color online). $\tilde{D}^0 \to K_S^0 K^+ K^-$ Dalitz plot distributions for (a) $B^- \to \tilde{D}^0 K^-$, (b) $B^+ \to \tilde{D}^0 K^+$, (c) $B^- \to \tilde{D}^{*0}[\tilde{D}^0 \pi^0]K^-$, (d) $B^+ \to \tilde{D}^{*0}[\tilde{D}^0 \pi^0]K^+$, (e) $B^- \to \tilde{D}^{*0}[\tilde{D}^0 \gamma]K^-$, and (f) $B^+ \to \tilde{D}^{*0}[\tilde{D}^0 \gamma]K^+$, for the ΔE signal region. The requirements m_{ES} GeV/c^2 and $\mathcal{F} > -0.1$ have been applied to reduce the background contamination, mainly from continuum events. The contours (solid red lines) represent the kinematical limits of the $\tilde{D}^0 \to K_S^0 K^+ K^-$ decay.

$r_{B^-} = r_{B^+}$ is recovered in the statistical procedure to extract γ from $x_{\mp}$, $y_{\mp}$, as discussed in Sec. V. The same procedure is applied analogously to the other signal samples.

We consider the same background components as in the selection fit, with some important modifications. First, events falling into the continuum and $B\bar{B}$ background components are divided into events with a real or a fake (combinatorial) $\tilde{D}^0$ meson. Dalitz plot shapes for fake $\tilde{D}^0$

mesons from continuum are extracted as described in Sec. III B, using events in the continuum enriched region (m_{ES} and m_D sideband regions), while those from $B\bar{B}$ are determined from MC events. Events containing a real $\tilde{D}^0$ are further divided into "right-sign" and "wrong-sign" flavor categories depending on whether they are combined with a negative or positive kaon (or K^*). We pay special attention to this charge-flavor correlation in the background since it can mimic either the $b \to c$ or the $b \to u$ signal component. Second, we have included a background contribution due to signal events where the kaon (or K^*) comes from the other B decay; this amounts to 9% of the $B^- \to \tilde{D}^0 K^{*-}$ signal, but is negligible for $B^- \to \tilde{D}^{(*)0}K^-$.

The m_{ES}, ΔE, and $\mathcal{F}$ PDF parameters in the CP fit are the same as those used in or obtained from the selection fit, except for the m_{ES} peaking fractions for $\tilde{D}^0 \to K_S^0 \pi^+ \pi^-$ channels, which are allowed to vary since their values depend on the ΔE region used for the fit. Other parameters simultaneously determined from the fit, along with the CP-violating parameters $x_{\mp}^{(*)}$, $y_{\mp}^{(*)}$, $x_{s\mp}$, and $y_{s\mp}$, are as follows: signal and background yields, signal charge asymmetries, and fractions of true D^0 mesons for all decay modes and right-sign fractions for $\tilde{D}^0 \to K_S^0 \pi^+ \pi^-$ channels in continuum background. Right-sign fractions for the modes with $\tilde{D}^0 \to K_S^0 \pi^+ \pi^-$ are fixed from MC simulation due to lack of statistics and the limited discriminating power between D^0 and $\bar{D}^0$ Dalitz plot distributions. Similarly, fractions of true $\tilde{D}^0$ mesons and charge-flavor correlation for the $B\bar{B}$ component are determined using MC events, because of the lack of $B\bar{B}$ background statistics.

A. Results and cross-checks

We find 600 ± 31, 133 ± 15, 129 ± 16, and 118 ± 18 signal events, for $B^- \to \tilde{D}^0 K^-$, $B^- \to \tilde{D}^{*0}[\tilde{D}^0 \pi^0]K^-$, $B^- \to \tilde{D}^{*0}[\tilde{D}^0 \gamma]K^-$, and $B^- \to \tilde{D}^0 K^{*-}$ decay modes, respectively, with $\tilde{D}^0 \to K_S^0 \pi^+ \pi^-$. Similarly, for the $\tilde{D}^0 \to K_S^0 K^+ K^-$ channels we obtain 112 ± 13, 32 ± 7, and 21 ± 7 signal events, for $B^- \to \tilde{D}^0 K^-$, $B^- \to \tilde{D}^{*0}[\tilde{D}^0 \pi^0]K^-$, and $B^- \to \tilde{D}^{*0}[\tilde{D}^0 \gamma]K^-$. Errors are statistical only. No statistically significant charge asymmetries are observed. The results for the CP-violating parameters $x_{\mp}^{(*)}$, $y_{\mp}^{(*)}$, $x_{s\mp}$, and $y_{s\mp}$, are summarized in Table IV. The only nonzero statistical correlations involving the CP parameters are for the pairs (x_-, y_-), (x_+, y_+), (x_-^*, y_-^*), (x_+^*, y_+^*), (x_{s-}, y_{s-}),

TABLE IV. CP-violating parameters $x_{\mp}^{(*)}$, $y_{\mp}^{(*)}$, $x_{s\mp}$, and $y_{s\mp}$, as obtained from the CP fit. The first error is statistical, the second is experimental systematic uncertainty, and the third is the systematic uncertainty associated with the Dalitz models.

Parameters	$B^- \to \tilde{D}^0 K^-$	$B^- \to \tilde{D}^{*0} K^-$	$B^- \to \tilde{D}^0 K^{*-}$
x_-, x_-^*, x_{s-}	$0.090 \pm 0.043 \pm 0.015 \pm 0.011$	$-0.111 \pm 0.069 \pm 0.014 \pm 0.004$	$0.115 \pm 0.138 \pm 0.039 \pm 0.014$
y_-, y_-^*, y_{s-}	$0.053 \pm 0.056 \pm 0.007 \pm 0.015$	$-0.051 \pm 0.080 \pm 0.009 \pm 0.010$	$0.226 \pm 0.142 \pm 0.058 \pm 0.011$
x_+, x_+^*, x_{s+}	$-0.067 \pm 0.043 \pm 0.014 \pm 0.011$	$0.137 \pm 0.068 \pm 0.014 \pm 0.005$	$-0.113 \pm 0.107 \pm 0.028 \pm 0.018$
y_+, y_+^*, y_{s+}	$-0.015 \pm 0.055 \pm 0.006 \pm 0.008$	$0.080 \pm 0.102 \pm 0.010 \pm 0.012$	$0.125 \pm 0.139 \pm 0.051 \pm 0.010$

(x_{s+}, y_{s+}), which amount to 0.4%, 3.5%, -14.0%, -5.6%, -29.9%, and 6.8%, respectively. Figure 9 shows the 39.3% and 86.5% 2-dimensional confidence-level (CL) contours in the $(x_\mp, y_\mp)$, $(x_\mp^*, y_\mp^*)$, and $(x_{s\mp}, y_{s\mp})$ planes, corresponding to 1- and 2-standard-deviation regions (statistical only). The separation of the B^- and B^+ positions in the (x, y) plane is equal to $2r_B|\sin\gamma|$ and is a measurement of direct *CP* violation. The angle between the lines connecting the B^- and B^+ centers with the origin $(0, 0)$ is equal to 2γ.

A variety of studies using data, parametrized fast Monte Carlo, and full GEANT4-simulated samples have been performed to test the consistency of the results and to verify the analysis chain and fitting procedure, as described below.

The *CP* fit to the $B^- \to \tilde{D}^{(*)0}K^-$ samples has been performed separately for $\tilde{D}^0 \to K_S^0\pi^+\pi^-$ and $\tilde{D}^0 \to K_S^0K^+K^-$ samples. Figure 10 shows the resulting 1- and 2-standard-deviation regions in the $(x_\mp^{(*)}, y_\mp^{(*)})$ planes. We find statistically consistent results between the different subsets. The same fitting procedure has been applied to the $B^- \to D^{(*)0}\pi^-$ control samples. In this case we expect $r_{B,\pi}^{(*)} \approx |V_{cd}V_{ub}^*|/|V_{ud}V_{cb}^*|c_F$ to be approximately 0.01. Since the experimental resolutions on $(x_{\mp,\pi}^{(*)}, y_{\mp,\pi}^{(*)})$ are expected to have the same order of magnitude, the $(x_{\mp,\pi}^{(*)}, y_{\mp,\pi}^{(*)})$ contours for B^- and B^+ decays should be close to the origin up to ~ 0.01. Deviations from this pattern could be an indication that the Dalitz plot distributions are not well described by the models. Figure 11 shows the resulting 1- and 2-standard-deviation regions for $(x_{\mp,\pi}^{(*)}, y_{\mp,\pi}^{(*)})$, consistent with the expected values. Moreover, we find statistically consistent results between the $D^0 \to K_S^0\pi^+\pi^-$ and $D^0 \to K_S^0K^+K^-$ samples.

An additional test of the fitting procedure is performed with parametrized MC simulations consisting of about 500 experiments generated with a sample size and composition corresponding to that of the data. The *CP* parameters are generated with values close to those found in the data and the reference *CP* fit is performed on each of these experi-

FIG. 10 (color online). Contours at 39.3% (dark) and 86.5% (light) 2-dimensional CL in the (a), (c) $(x_\mp, y_\mp)$ and (b), (d) $(x_\mp^*, y_\mp^*)$ planes, corresponding to 1- and 2-standard-deviation regions (statistical only), for $B^- \to \tilde{D}^{(*)0}K^-$ (thick and solid lines) and $B^+ \to \tilde{D}^{(*)0}K^+$ (thin and dotted lines) decays, for (a), (b) $\tilde{D}^0 \to K_S^0\pi^+\pi^-$ and (c), (d) $\tilde{D}^0 \to K_S^0K^+K^-$ only decay modes.

ments. The rms of the residual distributions for all the *CP* parameters (where the residual is defined as the difference between the fitted and generated values) is found to be consistent with the mean (Gaussian) statistical errors reported by the fits. The mean values of the residual distributions are consistent with zero. Only for $x_{s\mp}$ and $y_{s\mp}$ we observe small biases (at 10% level of the statistical uncertainty), as a consequence of the non-Gaussian behavior of samples with small statistics. This small deviation from Gaussian behavior is also observed in the data, as shown in

FIG. 9 (color online). Contours at 39.3% (dark) and 86.5% (light) 2-dimensional confidence level (CL) in the (a) $(x_\mp, y_\mp)$, (b) $(x_\mp^*, y_\mp^*)$, and (c) $(x_{s\mp}, y_{s\mp})$ planes, corresponding to 1- and 2-standard-deviation regions (statistical only), for B^- (thick and solid lines) and B^+ (thin and dotted lines) decays.
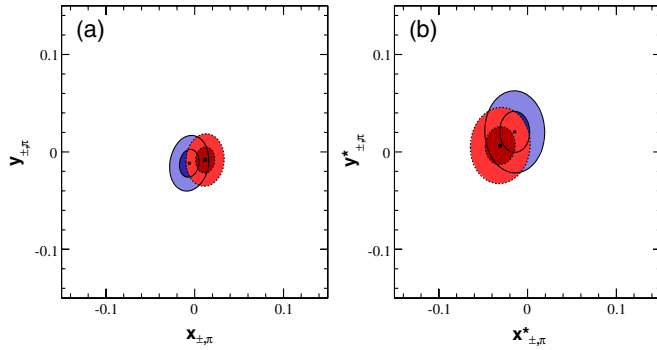
FIG. 11 (color online). Contours at 39.3% (dark) and 86.5% (light) 2-dimensional CL in the (a) $(x_{\mp,\pi}, y_{\mp,\pi})$ and (b) $(x^*_{\mp,\pi}, y^*_{\mp,\pi})$ planes, corresponding to 1- and 2-standard-deviation regions (statistical only), for $B^- \rightarrow D^{(*)0}\pi^-$ (thick and solid lines) and $B^+ \rightarrow \bar{D}^{(*)0}\pi^+$ (thin and dotted lines) control sample decays. Note the differences in scale when comparing to Figs. 9 and 10.

Fig. 9(c). The statistical errors on the *CP* parameters and the calculated correlation coefficients among them extracted from the fit are consistent with the range of values obtained from these experiments. We also observe that the fit errors are independent of the truth values.

Finally, samples of signal and background GEANT4-simulated MC events with a full detector simulation are used to validate the measurement. We performed fits to signal samples, using the true and reconstructed *B* meson charge and $\tilde{D}^0$ Dalitz plot distributions, obtaining in all cases results consistent with those generated.

B. Systematic uncertainties

1. Dalitz model contributions

Dalitz model uncertainties are evaluated by repeating the fit to the tagged D^0 samples with alternative assumptions to those adopted in the reference $D^0 \rightarrow K_S^0 \pi^+ \pi^-$ and $D^0 \rightarrow K_S^0 K^+ K^-$ amplitude analyses (Sec. III E), and then are propagated to the *CP* parameters. To propagate each

systematic uncertainty on $\mathcal{A}_D(\mathbf{m})$ to the *CP* parameters we have generated samples of $B^- \rightarrow \tilde{D}^{(*)0}K^-$ and $B^- \rightarrow \tilde{D}^0 K^{*-}$ signal events that are 100 times larger than each measured signal yield in data. These virtually infinite samples reduce to a negligible level statistical differences between the models. The D^0 Dalitz plot distributions are generated according to the reference models and to *CP* parameters consistent with the values found in data. The *CP* parameters are then extracted by fitting the generated Dalitz plot distributions using the reference or one of the alternative models. The difference is taken as the systematic uncertainty associated with each alternative model, and the sign of the variation is used to estimate whether the different contributions are positively or negatively correlated (see the Appendix). When two alternative models are built from an up and down variation of the same parameter, we take the maximum variation as the systematic error. Assuming the contributions are uncorrelated, we sum in quadrature to obtain the total systematic uncertainty.

The statistical errors in the Dalitz model parameters obtained from the tagged D^0 samples have been propagated to the *CP* parameters by repeating the *CP* fit with those parameters randomized according to their covariance matrix.

Table V summarizes the main contributions from all the alternative models considered and discussed in Sec. III E. Contributions from other models are found to be negligible.

We have also evaluated the effect on the measured *CP* parameters when we parametrize the $\pi\pi$ and $K\pi$ S waves in $D^0 \rightarrow K_S^0 \pi^+ \pi^-$ using the isobar model instead of the K-matrix model (plus the nonresonant contribution), as described in Sec. III C. The variations are found to be smaller than the sum of the $\pi\pi$ and $K\pi$ S-wave systematic uncertainties, and are used as a cross-check of the procedure adopted for assigning this contribution to the total Dalitz model error.

TABLE V. Summary of the main contributions to the Dalitz model systematic error on the *CP* parameters.

Source	x_-	y_-	x_+	y_+	x^*_-	y^*_-	x^*_+	y^*_+	x_{s-}	y_{s-}	x_{s+}	y_{s+}
Mass and width of Breit-Wigner's	0.001	0.001	0.001	0.002	0.001	0.002	0.001	0.003	0.003	0.001	0.002	0.002
$\pi\pi$ S-wave K-matrix solutions	0.003	0.012	0.003	0.001	0.003	0.007	0.002	0.009	0.001	0.001	0.013	0.003
$K\pi$ S-wave parametrization	0.001	0.001	0.002	0.004	0.001	0.003	0.001	0.003	0.005	0.001	0.004	0.002
Angular dependence	0.001	0.001	0.001	0.001	0.001	0.001	0.002	0.001	0.003	0.001	0.003	0.001
Blatt-Weisskopf radius	0.001	0.001	0.001	0.001	0.001	0.001	0.001	0.001	0.002	0.001	0.001	0.003
Add/remove resonances	0.001	0.001	0.001	0.001	0.001	0.002	0.001	0.002	0.001	0.001	0.001	0.002
Dalitz plot efficiency	0.006	0.004	0.008	0.001	0.002	0.004	0.002	0.003	0.008	0.001	0.008	0.004
Background Dalitz plot shape	0.003	0.002	0.004	0.001	0.001	0.001	0.001	0.001	0.004	0.001	0.004	0.002
Normalization and binning	0.001	0.001	0.001	0.002	0.001	0.001	0.001	0.002	0.002	0.001	0.003	0.001
Mistag rate	0.008	0.006	0.006	0.005	0.002	0.001	0.002	0.003	0.008	0.010	0.004	0.007
Dalitz plot complex amplitudes	0.002	0.002	0.003	0.004	0.001	0.001	0.002	0.006	0.003	0.003	0.004	0.002
Total Dalitz model	0.011	0.015	0.011	0.008	0.004	0.010	0.005	0.012	0.014	0.011	0.018	0.010

2. Experimental contributions

Experimental systematic uncertainties arise from several sources and their main contributions are summarized in Table VI. They are small compared to the statistical precision, and their sum is similar to the Dalitz model uncertainty. Other sources of experimental systematic uncertainty, e.g., the assumption of perfect mass resolution for the Dalitz plot variables **m**, are found to be negligible.

Statistical uncertainties due to the m_{ES}, ΔE, and $\mathcal{F}$ PDF parameters for signal and background extracted from the selection fit (fixed in the reference *CP* fit) are estimated by repeating the *CP* fit with PDF parameters randomized according to their covariance matrix. Possible bias due to differences in the m_{ES} and $\mathcal{F}$ shapes for continuum and $B\bar{B}$ background events between the ΔE selection and signal regions are evaluated applying the selection fit in the ΔE signal region. Other PDF parameters, such as the m_{ES} end point, $B\bar{B}$ ΔE peaking fractions, m_{ES} $B\bar{B}$ peaking fractions for $\tilde{D}^0 \to K_S^0 K^+ K^-$ channels, and PEP-II boost are varied by 1 standard deviation. We account for m_{ES} and ΔE differences in $B\bar{B}$ background for true and fake D mesons, while for continuum events we do not observe differences. We also find the effect of the small correlation between m_{ES}, ΔE, and $\mathcal{F}$ variables negligible.

The uncertainties related to the knowledge of the $\tilde{D}^0$ fractions for the small $B\bar{B}$ background are estimated from the maximum variations of the *CP* parameters when the fractions are varied 1σ up and down from their MC estimates, or replaced by the values found for the continuum background, or assumed to be zero. Similarly, the uncertainties due to our knowledge of the right-sign fractions for $\tilde{D}^0 \to K_S^0 K^+ K^-$ continuum events and $B\bar{B}$ events are evaluated from the maximum variations of the *CP* parameters after varying these fractions according to their MC values or assuming that the $\tilde{D}^0$ is randomly associated either with a negatively or positively charged kaon (absence of correlation).

The effect due to reconstruction efficiency variations of the signal across the Dalitz plane, $\epsilon(\mathbf{m})$, has been evaluated by varying randomly the coefficients of the polynomial parametrization according to their covariance matrix, in-

cluding the statistical errors due to the limited MC statistics as well as systematic uncertainties arising from the imperfections of the detector simulation, as discussed in Sec. III E 2.

The uncertainty associated with the knowledge of the Dalitz plot distributions of continuum background events is taken to be the difference in the *CP* parameters using background Dalitz plot shapes from sideband data instead of signal region backgrounds from MC. We also account for statistical uncertainties adding in quadrature the rms of the distributions of *CP* parameters when the two sets of profile distributions are randomized. Uncertainties due to the Dalitz plot shapes of combinatorial D mesons in $B\bar{B}$ background are conservatively estimated from the variation of *CP* parameters when the reference shapes are replaced by a flat profile.

The effect of the remaining cross feed of $B^- \to \tilde{D}^{*0}[\tilde{D}^0\pi^0]K^-$ events into the $B^- \to \tilde{D}^{*0}[\tilde{D}^0\gamma]K^-$ sample (5% of the signal yield) has been evaluated by including in the *CP* fit an additional background component to the latter sample with $\mathcal{P}_c(\mathbf{m}_j)$ identical to that of the signal component of the former.

Possible *CP*-violating effects in the background have been evaluated by setting the *CP* parameters of the $B^- \to D^{(*)0}\pi^-$ background component to the values obtained from a *CP* fit to the $B^- \to D^{(*)0}\pi^-$ control samples, and by floating an independent set of *CP* parameters for the mixture of $B\bar{B}$ background.

The $B^- \to \tilde{D}^0 K^{*-}$ sample has two additional sources of uncertainty. The first one comes from signal events where the prompt K^{*-} is replaced by a combinatorial K^{*-} (about 9% of the signal), with either the same or opposite charge. This systematic uncertainty, evaluated by changing by $\pm 10\%$ the fraction of these events and neglecting the charge-flavor correlation, has been found to be negligible.

The second additional uncertainty is due to our knowledge of the parameter κ, as defined in Eq. (3), which accounts for the interference between $B^- \to \tilde{D}^0 K^{*-}$ and other $B^- \to \tilde{D}^0 K_S^0 \pi^-$ (higher K^* resonances plus nonresonant) decays. Since this parameter cannot be extracted from the *CP* fit and no experimental data analysis is

TABLE VI. Summary of the main contributions to the experimental systematic error on the *CP* parameters.

Source	x_-	y_-	x_+	y_+	x_-^*	y_-^*	x_+^*	y_+^*	x_{s-}	y_{s-}	x_{s+}	y_{s+}
m_{ES}, ΔE, $\mathcal{F}$ shapes	0.001	0.001	0.001	0.002	0.002	0.004	0.004	0.005	0.003	0.002	0.001	0.004
Real D^0 fractions	0.001	0.001	0.001	0.001	0.001	0.001	0.004	0.001	0.002	0.004	0.001	0.001
Charge-flavor correlation	0.002	0.002	0.001	0.001	0.002	0.002	0.002	0.001	0.001	0.002	0.001	0.001
Efficiency in the Dalitz plot	0.002	0.002	0.002	0.002	0.001	0.001	0.001	0.001	0.002	0.003	0.001	0.005
Background Dalitz plot shape	0.012	0.007	0.013	0.003	0.010	0.007	0.007	0.007	0.014	0.006	0.012	0.005
$B^- \to D^{*0}K^-$ cross feed	$\cdots$	$\cdots$	$\cdots$	$\cdots$	0.003	0.002	0.007	0.001	$\cdots$	$\cdots$	$\cdots$	$\cdots$
CP violation in $D\pi$ and $B\bar{B}$ bkg	0.001	0.001	0.001	0.001	0.005	0.001	0.001	0.004	0.006	0.002	0.003	0.001
Non-K^* $B^- \to \tilde{D}^0 K_S^0 \pi^-$ decays	$\cdots$	$\cdots$	$\cdots$	$\cdots$	$\cdots$	$\cdots$	$\cdots$	$\cdots$	0.035	0.058	0.025	0.045
Total experimental	0.015	0.007	0.014	0.006	0.014	0.009	0.014	0.010	0.039	0.058	0.028	0.051

available on the $B^- \to \tilde{D}^0 K_S^0 \pi^-$ decay, we study a B^- Dalitz (isobar) model including $K^*(892)^-$, $K_0^*(1410)^-$, $K_2^*(1430)^-$, $D^*(2010)^-$, $D_2^*(2460)^-$ and nonresonant terms, and randomly varying phases in the range $[0, 2\pi)$ and magnitudes [50]. The magnitude of the contribution from $b \to c$ transitions relative to $b \to u$ was fixed to be around 3, while the magnitude of the nonresonant contribution was varied between 0 and 1. Since our model has a large uncertainty we made several alternative models adding/removing resonances and changing ranges for $b \to u$ amplitudes, keeping the K^* pollution (defined as the non-K^* fit fraction) below 5%–10%, since from earlier studies with very similar selection criteria we estimate that, neglecting higher resonances, the nonresonant K^* decays contribute about 5% of the signal events [51]. Evaluating κ from Eq. (3) for the region within 55 MeV/c^2 of the K^* mass and $|\cos\theta_H| \geq 0.35$ we find quite narrow distributions, centered around 0.9 and with rms not larger than 0.1, in agreement with previous studies [52]. For this reason we have fixed the value of κ to 0.9 in the reference CP fit, and varied it between 0.8 and 1.

V. INTERPRETATION OF RESULTS

A frequentist procedure [21] has been adopted to transform the measurement of the CP parameters $\mathbf{z}_{\mp} \equiv (x_\mp, y_\mp, x_\mp^*, y_\mp^*, x_{s\mp}, y_{s\mp})$ into the measurement of the physically relevant quantities $\mathbf{p} \equiv (\gamma, r_B, r_B^*, \kappa r_s, \delta_B, \delta_B^*, \delta_s)$.

Using a large number of pseudoexperiments with probability density functions and parameters as obtained from the fit to the data but with different values of the CP parameters, we construct a multivariate Gaussian likelihood function $\mathcal{L}(\mathbf{p} \mid \mathbf{z}, \mathcal{C})$ relating the experimentally measured observables $\mathbf{z} \equiv \{\mathbf{z}_+, \mathbf{z}_-\}$ (reported in Table IV) and their 12×12 statistical and systematic covariance matrices $\mathcal{C}$ with the corresponding true values calculated using their definition in terms of the quantities $\mathbf{p}$. The matrices $\mathcal{C}$ are constructed from the uncertainties summarized in Table IV and the statistical and systematic correlation coefficients given in Sec. IVA and the Appendix, respectively. For a single B decay channel the procedure is identical to that outlined here but with a reduced space of measured and truth parameters. For example, for $B^- \to \tilde{D}^0 K^-$, $\mathbf{z}_\pm \equiv (x_\pm, y_\pm)$, $\mathcal{C}$ is the corresponding 4×4 covariance matrix, and $\mathbf{p} \equiv (\gamma, r_B, \delta_B)$.

We evaluate the CL as a function of the true value for a given parameter μ from $\mathbf{p} \equiv \{\mu, \mathbf{q}\}$, minimizing the function $\chi^2(\mathbf{p} \mid \mathbf{z}, \mathcal{C}) \equiv -2\ln\mathcal{L}(\mathbf{p} \mid \mathbf{z}, \mathcal{C})$ with respect to the parameters $\mathbf{q}$. For each given value μ_0 of μ, between its minimum and maximum values, the fit provides a minimum chi square $\chi^2(\mu_0, \mathbf{q_0})$, where $\mathbf{q_0}$ are the best parameters for the given μ_0 and the actual $\mathbf{z}$ measurements with covariance matrix $\mathcal{C}$. Then we take the values $\mathbf{p}_{\text{best}} \equiv \{\mu_{\text{best}}, \mathbf{q}_{\text{best}}\}$ for which $\chi^2(\mu_{\text{best}}, \mathbf{q}_{\text{best}})$ is minimum and

compute the χ^2 difference $\Delta\chi^2(\mu_0) = \chi^2(\mu_0, \mathbf{q}_0) - \chi^2(\mu_{\text{best}}, \mathbf{q}_{\text{best}})$.

In a purely Gaussian situation for the truth parameters $\mathbf{p}$, the CL can be obtained by computing the probability that this value is exceeded for a χ^2 distribution with 1 degree of freedom, CL $= 1 - \alpha = F(\Delta\chi^2(\mu_0); \nu = 1)$, where $F(\Delta\chi^2(\mu_0); \nu = 1)$ is the corresponding cumulative distribution function. In a non-Gaussian situation one has to consider $\Delta\chi^2(\mu_0)$ as a test statistic, and has to rely on a Monte Carlo simulation to obtain its expected distribution. This Monte Carlo simulation is built by generating a large number of samples with truth values $\mathbf{p_0} \equiv \{\mu_0, \mathbf{q_0}\}$ as determined from the actual data analysis, and then counting the number of experiments for which $\Delta\chi'^2(\mu_0) < \Delta\chi^2(\mu_0)$, where $\Delta\chi'^2(\mu_0) = \chi'^2(\mu_0, \mathbf{q}_0') - \chi'^2(\mu_{\text{best}}', \mathbf{q}_{\text{best}}')$ is determined by letting the $\mathbf{q}$ parameters free to vary for each of the generated (primed) samples. The 1-(2-) standard-deviation regions of the CP parameters are defined as the set of μ_0 values for which α is greater than 31.7% (4.6%).

This technique to obtain the physical parameters takes into account unphysical regions of the parameter space [53], which may arise since in the $\mathbf{z}$ measurements we allow B^- and B^+ events to have different r_{B^-} and r_{B^+} values, while the space of true values is built using a common r_B parameter. Moreover, this approach provides 1-dimensional intervals that include the true value as implied by the confidence level, while in previous measure-
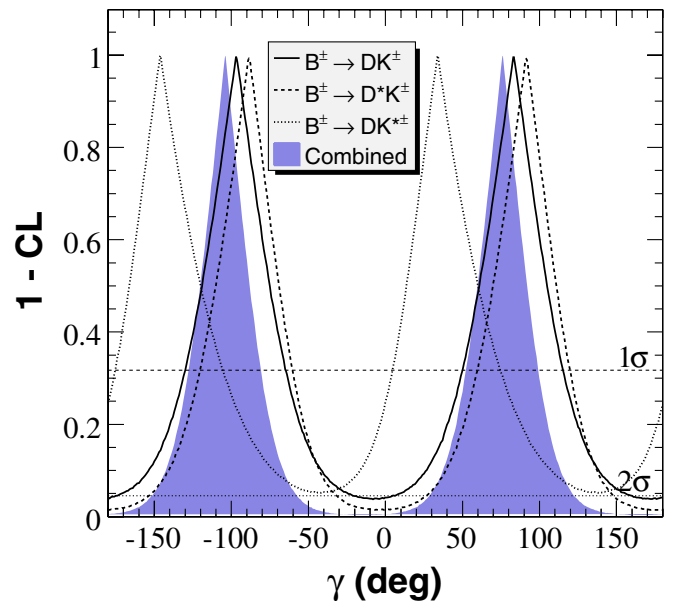
FIG. 12 (color online). $\alpha = 1 -$ CL as a function of γ for $B^- \to \tilde{D}^0 K^-$, $B^- \to \tilde{D}^{*0} K^-$, and $B^- \to \tilde{D}^0 K^{*-}$ decays separately, and their combination, including statistical and systematic uncertainties and their correlations. The dashed (upper) and dotted (lower) horizontal lines correspond to the 1- and 2- standard-deviation intervals, respectively.

ments [18,54] the 1-dimensional intervals were determined from projections of the multidimensional confidence regions onto each of the parameters.

Figure 12 shows $\alpha = 1 - CL$ as a function of the parameter γ, for each of the three B decay channels separately and their combination. As expected from Eq. (2), the method has a twofold ambiguity in the weak and strong phases, $(\gamma; \delta_B^{(*)}, \delta_s) \rightarrow (\gamma + 180°; \delta_B^{(*)} + 180°, \delta_s + 180°)$. For the combination of all decay modes we obtain $\gamma = (76^{+23}_{-24})° \{5, 5\}°$ (mod 180°), where the error includes
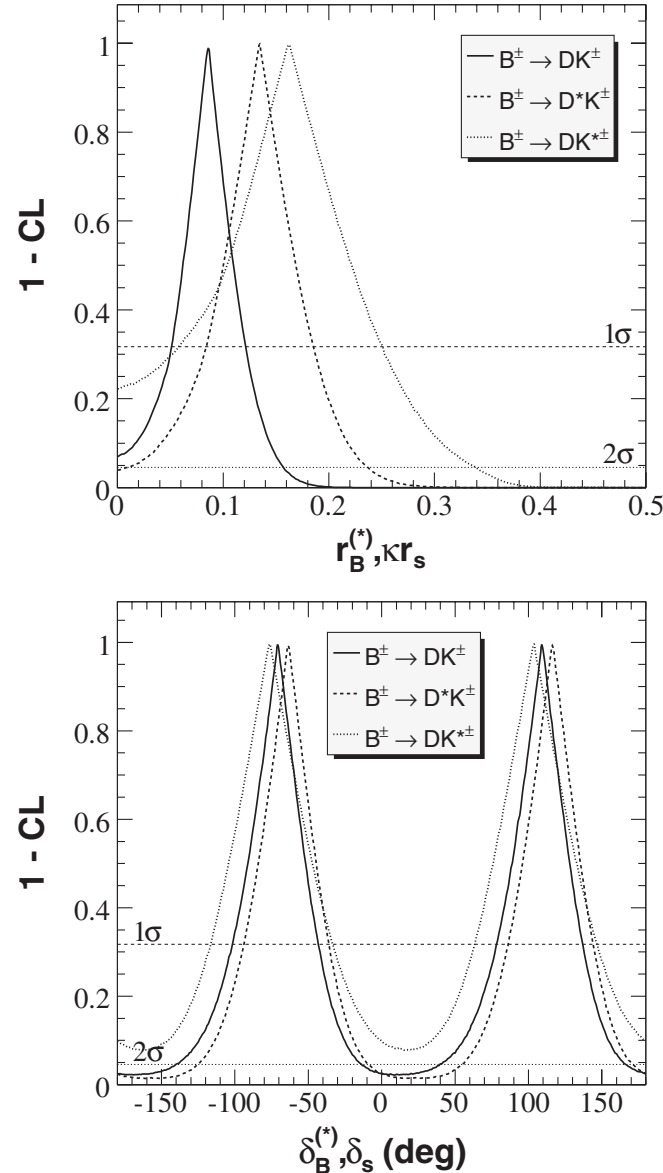
statistical, experimental, and Dalitz model systematic uncertainties. The values inside brackets indicate the parabolic contributions to the total error coming from experimental and Dalitz model systematic uncertainties. The corresponding 2-standard-deviation interval is [29, 122]°. The central value is taken at the point of maximum α, including all sources of uncertainties. Considering only $D^0 \rightarrow K_S^0 \pi^+ \pi^-$ samples we obtain $\gamma = (63^{+30}_{-28})° \{8, 7\}° [5, 125]°$ (mod 180°).

Similarly, Fig. 13 shows α as a function of the amplitude ratios r_B, r_B^*, and κr_s, and the strong phases δ_B, δ_B^*, and δ_s. We obtain $r_B = 0.086 \pm 0.035 \{0.010, 0.011\}$, $r_B^* = 0.135 \pm 0.051 \{0.011, 0.005\}$, $\kappa r_s = 0.163^{+0.088}_{-0.105} \{0.037, 0.021\}$ $(r_s = 0.181^{+0.100}_{-0.118})$, $\delta_B = (109^{+28}_{-31})° \{4, 7\}°$, $\delta_B^* = (-63^{+28}_{-30})° \{5, 4\}°$, and $\delta_s = (104^{+43}_{-41})° \{17, 5\}°$. The results of the strong phases correspond to the solution for γ in the sheet [0, 180]°. The corresponding 2-standard-deviation intervals are $r_B < 0.157$, $r_B^* \in [0.011, 0.237]$, $\kappa r_s < 0.338$ $(r_s < 0.377)$, $\delta_B \in [40, 166]°$, and $\delta_B^* \in [-125, -9]°$. No constraint on δ_s is achieved at the 2-standard-deviation level.

The significance of direct CP violation is obtained by evaluating the $CL = 1 - \alpha$ for the most probable CP conserving point, i.e., the set of coordinates of **p** with minimum CL and $\gamma = 0$. Including statistical and systematic uncertainties, we obtain CL = 0.971, 0.989, and 0.871, corresponding to 2.2, 2.5, and 1.5 standard deviations, for $B^- \rightarrow \tilde{D}^0 K^-$, $B^- \rightarrow \tilde{D}^{*0} K^-$, and $B^- \rightarrow \tilde{D}^0 K^{*-}$ decays, respectively. For the combined analysis of the three charged $B \rightarrow DK$ decay modes we obtain CL = 0.997, corresponding to 3.0 standard deviations.

VI. CONCLUSION

In summary, using $383 \times 10^6 B\bar{B}$ decays recorded by the *BABAR* detector, we have performed a new measurement of the direct CP-violating parameters $(x_\mp^{(*)}, y_\mp^{(*)})$ and $(x_{s\mp}, y_{s\mp})$ in $B^- \rightarrow \tilde{D}^{(*)0} K^-$ and $B^- \rightarrow \tilde{D}^0 K^{*-}$ decays, respectively, using a Dalitz plot analysis of $\tilde{D}^0 \rightarrow K_S^0 \pi^+ \pi^-$ and $\tilde{D}^0 \rightarrow K_S^0 K^+ K^-$. Compared to our previous analysis based on $227 \times 10^6 B\bar{B}$ decays [18], this measurement takes advantage of significant improvements in reconstruction efficiencies, treatment of $e^+ e^- \rightarrow q\bar{q}$, $q = u$, d, s, c backgrounds, and Dalitz models, along with the use, for the first time, of $\tilde{D}^0 \rightarrow K_S^0 K^+ K^-$ decays. These upgrades result in reduced experimental and Dalitz model systematic uncertainties, and statistical uncertainties improved beyond the increase in data sample size. The results, summarized in Table IV are consistent with, and improve significantly, the previous measurements from *BABAR* and Belle [18,54].

A significant reduction in Dalitz model systematic uncertainties has been achieved through the detailed study of high-statistics samples of $e^+ e^- \rightarrow c\bar{c} \rightarrow D^{*+} \rightarrow D^0 \pi^+$

FIG. 13. $\alpha = 1 - CL$ as a function of (upper panel) r_B, r_B^*, and κr_s, and (lower panel) δ_B, δ_B^*, and δ_s, for $B^- \rightarrow \tilde{D}^0 K^-$, $B^- \rightarrow \tilde{D}^{*0} K^-$, and $B^- \rightarrow \tilde{D}^0 K^{*-}$ decays, including statistical and systematic uncertainties and their correlations. The dashed (upper) and dotted (lower) horizontal lines correspond to the 1- and 2-standard-deviation intervals, respectively.

decays, where the D^0 is reconstructed in the $K_S^0 \pi^+ \pi^-$ and $K_S^0 K^+ K^-$ final states. We have adopted a K-matrix formalism to describe the complex $\pi\pi$ and $K\pi$ S-wave dynamics in $D^0 \to K_S^0 \pi^+ \pi^-$. For this decay, the fit fractions measured and reported in Table II show that the $K\pi$ and $\pi\pi$ P waves dominate, but for the first time significant contributions from the corresponding S waves are observed (above 6 and 4 standard deviations, respectively).

Using a frequentist analysis we interpret the $(x_\mp^{(*)}, y_\mp^{(*)})$ and $(x_{s\mp}, y_{s\mp})$ experimental results in terms of the weak phase γ, the amplitude ratios r_B, r_B^*, and r_s, and the strong phases δ_B, δ_B^*, and δ_s. We obtain $\gamma = (76 \pm 22 \pm 5 \pm 5)°$ (mod $180°$), where the first error is statistical, the second is the experimental systematic uncertainty, and the third reflects the uncertainty on the D decay Dalitz models (parabolic errors). The corresponding 2-standard-deviation region is $29° < \gamma < 122°$. The combined significance of direct CP violation (i.e., $\gamma \neq 0$) is 99.7%, corresponding to 3.0 standard deviations. This direct determination of γ supersedes and significantly improves our previous constraint [18], and is consistent with that reported by the Belle Collaboration [54]. The latter has a slightly better precision in spite of a larger uncertainty on the measured CP parameters because the error on γ scales roughly as $1/r_B^{(*)}(1/r_s)$ and our tighter $r_B^{(*)}$, κr_s constraints favor smaller values.

ACKNOWLEDGMENTS

APPENDIX: CORRELATION MATRICES

Averaging $x_\mp^{(*)}$, $y_\mp^{(*)}$, $x_{s\mp}$, and $y_{s\mp}$ measurements between different methods and experiments, and transforming into the physically relevant quantities $\mathbf{p} \equiv (\gamma, r_B, r_B^*, \kappa r_s, \delta_B, \delta_B^*, \delta_s)$ requires a complete evaluation of the different sources of uncertainties and their correlations. The statistical correlation coefficients are extracted from the fit and are reported in Sec. IV A. The experimental systematic and Dalitz model correlation coefficients for the measurement vector

$$\mathbf{z} \equiv (x_-, y_-, x_+, y_+, x_-^*, y_-^*, x_+^*, y_+^*, x_{s-}, y_{s-}, x_{s+}, y_{s+}),$$

are defined in the usual way as $\rho_{ij} = \mathcal{C}_{ij}/\sqrt{\mathcal{C}_{ii}\mathcal{C}_{jj}}$, where $\mathcal{C}_{ij} = \overline{(\mathbf{z} - \mathbf{z}_{\text{best}})_i (\mathbf{z} - \mathbf{z}_{\text{best}})_j}$, with $\mathbf{z}_{\text{best}}$ the vector of best measurements, and equal to (only diagonal and lower off-diagonal terms are written, in %):

$$\rho_{\text{exp}} = \begin{pmatrix}
100 \\
-2.2 & 100 \\
8.1 & 1.9 & 100 \\
22.4 & 3.4 & 12.7 & 100 \\
5.2 & -3.2 & 1.3 & 5.8 & 100 \\
-6.8 & 1.4 & -3.6 & -9.8 & -8.0 & 100 \\
-0.7 & -1.9 & -2.0 & 1.3 & 29.2 & -26.8 & 100 \\
-6.8 & -0.2 & -3.3 & -8.6 & -29.5 & 6.5 & -15.8 & 100 \\
0.0 & -1.0 & -0.4 & -2.2 & 6.2 & -0.4 & -0.2 & -6.4 & 100 \\
0.9 & 0.0 & 0.9 & 1.4 & -1.9 & -0.5 & -1.4 & 1.8 & 6.5 & 100 \\
-4.0 & -1.0 & -2.5 & -7.3 & 3.8 & 2.6 & -0.4 & -1.8 & -1.9 & -6.9 & 100 \\
-0.3 & -0.7 & -0.5 & -1.3 & 1.7 & 1.9 & 0.3 & -0.2 & -4.4 & -7.8 & 5.1 & 100
\end{pmatrix},$$

$$\rho_{\text{model}} = \begin{pmatrix}
100 \\
71.6 & 100 \\
90.5 & 64.9 & 100 \\
39.1 & 12.3 & 30.4 & 100 \\
-30.1 & -54.1 & -2.0 & -13.3 & 100 \\
-52.0 & -83.1 & -50.7 & 33.9 & 40.8 & 100 \\
-7.1 & -33.9 & -29.8 & 28.7 & -36.5 & 42.8 & 100 \\
51.2 & 77.4 & 45.0 & -22.9 & -48.7 & -86.2 & -30.0 & 100 \\
83.5 & 43.2 & 85.6 & 55.2 & 6.4 & -14.4 & -14.5 & 15.7 & 100 \\
59.3 & 28.4 & 34.6 & 57.4 & -51.3 & -0.9 & 55.4 & 12.6 & 43.4 & 100 \\
73.6 & 86.3 & 77.6 & 15.0 & -24.9 & -70.7 & -50.1 & 62.9 & 61.6 & 8.3 & 100 \\
42.6 & 39.2 & 19.8 & 64.6 & -66.2 & 1.3 & 41.2 & 10.3 & 30.8 & 68.9 & 26.9 & 100
\end{pmatrix}.$$

[1] N. Cabibbo, Phys. Rev. Lett. **10**, 531 (1963); M. Kobayashi and T. Maskawa, Prog. Theor. Phys. **49**, 652 (1973).

[2] A. Höcker and Z. Ligeti, Annu. Rev. Nucl. Part. Sci. **56**, 501 (2006); J. Charles *et al.*, Eur. Phys. J. C **41**, 1 (2005); A. Höcker *et al.*, Eur. Phys. J. C **21**, 225 (2001) and updates at http://ckmfitter.in2p3.fr/; M. Bona *et al.*, J. High Energy Phys. 07 (2005) 028; 03 (2006) 080 and updates at http://www.utfit.org/; F. J. Botella, G. C. Branco, and M. Nebot, Nucl. Phys. **B768**, 1 (2007).

[3] The symbols $D^{(*)}$ ($K^{(*)}$) refer to either a $D(K)$ or a $D^*(K^*)$ meson.

[4] $K^{*\mp}$ (and K^*) refers to $K^*(892)^{\mp}$.

[5] Reference to the charge-conjugate state is implied here and throughout the text unless otherwise specified.

[6] M. Gronau and D. London, Phys. Lett. B **253**, 483 (1991); M. Gronau and D. Wyler, Phys. Lett. B **265**, 172 (1991).

[7] D. Atwood, I. Dunietz, and A. Soni, Phys. Rev. Lett. **78**, 3257 (1997); Phys. Rev. D **63**, 036005 (2001).

[8] A. Giri, Y. Grossman, A. Soffer, and J. Zupan, Phys. Rev. D **68**, 054018 (2003).

[9] A. Poluetkov *et al.* (Belle Collaboration), Phys. Rev. D **70**, 072003 (2004).

[10] T. E. Browder, K. Honscheid, and D. Pedrini, Annu. Rev. Nucl. Part. Sci. **46**, 395 (1996).

[11] M. Gronau, Phys. Lett. B **557**, 198 (2003).

[12] R. H. Dalitz, Philos. Mag. **44**, 1068 (1953).

[13] H. Muramatsu *et al.* (CLEO Collaboration), Phys. Rev. Lett. **89**, 251802 (2002); **90**, 059901(E) (2003).

[14] B. Aubert *et al.* (*BABAR* Collaboration), Phys. Rev. Lett. **98**, 211802 (2007); M. Staric *et al.* (Belle Collaboration), Phys. Rev. Lett. **98**, 211803 (2007).

[15] Y. Grossman, A. Soffer, and J. Zupan, Phys. Rev. D **72**, 031501 (2005).

[16] L. M. Zhang *et al.* (Belle Collaboration), Phys. Rev. Lett. **99**, 131803 (2007).

[17] A. Bondar and T. Gershon, Phys. Rev. D **70**, 091503 (2004).

[18] B. Aubert *et al.* (*BABAR* Collaboration), Phys. Rev. Lett. **95**, 121802 (2005).

[19] a_1^- refers to $a_1(1260)^-$.

[20] B. Aubert *et al.* (*BABAR* Collaboration), Nucl. Instrum. Methods Phys. Res., Sect. A **479**, 1 (2002).

[21] W.-M. Yao *et al.* (Particle Data Group), J. Phys. G **33**, 1 (2006).

[22] R. A. Fisher, Annals Eugen. **7**, 179 (1936).

[23] S. Brandt, C. Peyrou, R. Sosnowski, and A. Wroblewski, Phys. Lett. **12**, 57 (1964); E. Farhi, Phys. Rev. Lett. **39**, 1587 (1977).

[24] M. E. Peskin and D. V. Schroeder, *An Introduction To Quantum Field Theory* (Addison-Wesley, Reading, MA, 1995).

[25] H. Albrecht *et al.* (ARGUS Collaboration), Z. Phys. C **48**, 543 (1990).

[26] M. Bauer *et al.*, Z. Phys. C **34**, 103 (1987).

[27] Review on Dalitz plot analysis formalism in Ref. [21].

[28] J. M. Blatt and V. F. Weisskopf, *Theoretical Nuclear Physics* (Wiley, New York, 1952).

[29] G. J. Gounaris and J. J. Sakurai, Phys. Rev. Lett. **21**, 244 (1968).

[30] C. Zemach, Phys. Rev. **133**, B1201 (1964); **140**, B97 (1965).

[31] V. Filippini, A. Fontana, and A. Rotondi, Phys. Rev. D **51**, 2247 (1995).

[32] M. Jacob and G. C. Wick, Ann. Phys. (Paris) **7**, 404 (1959); S. U. Chung *et al.*, Phys. Rev. D **48**, 1225 (1993).

[33] S. Kopp *et al.* (CLEO Collaboration), Phys. Rev. D **63**, 092001 (2001).

[34] The labels A and B should be swapped in Eq. (6) of Ref. [33].

[35] Review on scalar mesons in Ref. [21].

[36] E. P. Wigner, Phys. Rev. **70**, 15 (1946); S. U. Chung *et al.*, Ann. Phys. (Paris) **507**, 404 (1995).

[37] I. J. R. Aitchison, Nucl. Phys. **A189**, 417 (1972).

[38] D. Aston *et al.* (LASS Collaboration), Nucl. Phys. **B296**, 493 (1988).

[39] V. V. Anisovich and A. V. Sarantsev, Eur. Phys. J. A **16**, 229 (2003).

[40] J. M. Link *et al.* (FOCUS Collaboration), Phys. Lett. B **585**, 200 (2004).

[41] S. L. Adler, Phys. Rev. **137**, B1022 (1965).

[42] Y. P. Lau, Ph.D. dissertation, Princeton University, 2007.

[43] E. M. Aitala *et al.* (E791 Collaboration), Phys. Rev. D **73**, 032004 (2006); J. M. Link *et al.* (FOCUS Collaboration), Phys. Lett. B **653**, 1 (2007); G. Bonvicini *et al.* (CLEO Collaboration), arXiv:0802.4214 [Phys. Rev. D. (to be published)].

[44] E. M. Aitala *et al.* (E791 Collaboration), Phys. Rev. Lett. **89**, 121801 (2002).

[45] E. M. Aitala *et al.* (E791 Collaboration), Phys. Rev. Lett. **86**, 765 (2001).

[46] B. Aubert *et al.* (*BABAR* Collaboration), Phys. Rev. D **72**, 052008 (2005).

[47] A. Abele *et al.* (Crystall Barrel Collaboration), Phys. Rev. D **57**, 3860 (1998).

[48] M. Ablikim *et al.* (BES Collaboration), Phys. Lett. B **607**, 243 (2005).

[49] T. A. Armstrong *et al.* (WA76 Collaboration), Z. Phys. C **51**, 351 (1991).

[50] R. Aleksan, T. C. Petersen, and A. Soffer, Phys. Rev. D **67**, 096002 (2003).

[51] B. Aubert *et al.* (*BABAR* Collaboration), Phys. Rev. D **73**, 111104 (2006).

[52] B. Aubert *et al.* (*BABAR* Collaboration), Phys. Rev. D **72**, 071103 (2005); **72**, 071104 (2005).

[53] G. J. Feldman and R. D. Cousins, Phys. Rev. D **57**, 3873 (1998).

[54] A. Poluetkov *et al.* (Belle Collaboration), Phys. Rev. D **73**, 112009 (2006).